



ALMA MATER STUDIORUM
UNIVERSITÀ DI BOLOGNA

ARCHIVIO ISTITUZIONALE
DELLA RICERCA

Alma Mater Studiorum Università di Bologna Archivio istituzionale della ricerca

Flow pathways in multiple-direction fold hinges: Implications for fractured and karstified carbonate reservoirs

This is the final peer-reviewed author's accepted manuscript (postprint) of the following publication:

Published Version:

Pontes, C.C., Bezerra, F.H., Bertotti, G., La Bruna, V., Audra, P., De Waele, J.o., et al. (2021). Flow pathways in multiple-direction fold hinges: Implications for fractured and karstified carbonate reservoirs. JOURNAL OF STRUCTURAL GEOLOGY, 146, 1-19 [10.1016/j.jsg.2021.104324].

Availability:

This version is available at: <https://hdl.handle.net/11585/817625> since: 2021-03-31

Published:

DOI: <http://doi.org/10.1016/j.jsg.2021.104324>

Terms of use:

Some rights reserved. The terms and conditions for the reuse of this version of the manuscript are specified in the publishing policy. For all terms of use and more information see the publisher's website.

This item was downloaded from IRIS Università di Bologna (<https://cris.unibo.it/>).
When citing, please refer to the published version.

(Article begins on next page)

This is the final peer-reviewed accepted manuscript of:

Pontes, Cayo C.C.; Bezerra, Francisco H.R.; Bertotti, Giovanni; La Bruna, Vincenzo; Audra, Philippe; De Waele, Jo; Auler, Augusto S.; Balsamo, Fabrizio; De Hoop, Stephan; Pisani, Luca: *Flow pathways in multiple-direction fold hinges: Implications for fractured and karstified carbonate reservoirs*

JOURNAL OF STRUCTURAL GEOLOGY

VOL. 146

ISSN 0191-8141

DOI: 10.1016/j.jsg.2021.104324

The final published version is available online at:

<https://dx.doi.org/10.1016/j.jsg.2021.104324>

Terms of use:

Some rights reserved. The terms and conditions for the reuse of this version of the manuscript are specified in the publishing policy. For all terms of use and more information see the publisher's website.

This item was downloaded from IRIS Università di Bologna (<https://cris.unibo.it/>)

When citing, please refer to the published version.

1 **Flow pathways in multiple-direction fold hinges: Implications for fractured**
2 **and karstified carbonate reservoirs**

3
4 Cayo C. C. PONTES^{1*}, Francisco H. R. BEZERRA¹, Giovanni BERTOTTI²,
5 Vincenzo LA BRUNA¹, Philippe AUDRA³, Jo DE WAELE⁴, Augusto S.
6 AULER⁵, Fabrizio BALSAMO⁶, Stephan DE HOOP², Luca PISANI⁴.

7 1 Dept. of Geology, Federal University of Rio Grande do Norte, Natal, Brazil

8 2 Dept. of Geoscience and Engineering, Delft University of Technology, Delft, The Netherlands

9 3 Polytech'Lab EA 7498, University Côte d'Azur, France

10 4 Bologna University, Department of Biological, Geological and Environmental Sciences, Via Zamboni
11 67, 40126 Bologna, Italy

12 5 Instituto do Carste, Carste Ciência e Meio Ambiente, Belo Horizonte, Brazil

13 6 NEXT - Natural and Experimental Tectonic Research Group, Department of Chemistry, Life
14 Sciences and Environmental Sustainability, University of Parma, Italy

15

16 **Abstract**

17 Caves developed in carbonate units have a significant role in fluid flow, but most of
18 these subsurface voids are below seismic resolution. We concentrated our study on
19 four caves to determine the roles of fractures and folds in the development of karst
20 conduits that may form flow pathways in carbonate reservoirs. We performed structural
21 field investigations, petrographic analyses, and geometric characterization using Light
22 Detection and Ranging (LIDAR) for caves in Neoproterozoic carbonates of the Salitre
23 Formation, central part of the São Francisco Craton, Brazil. We found that the conduit
24 shape, usually with an ellipsoidal cross-section, is a reflection of the tectonic features
25 and textural variations. Carbonate layers containing pyrite and low contents of detritic

26 minerals are generally karstified and appear to act as favorable flow pathways. Our
27 results indicate that the development of the karst system is related to fracture corridors
28 formed along parallel and orthogonal sets of fold hinges, which provide preferential
29 pathways for fluid flow and contribute to the development of super-K zones. This study
30 provides insights about the prediction of subseismic-scale voids in subsurface
31 carbonate reservoirs, with direct application for the hydrocarbon and hydrogeology
32 communities.

33

34 **Keywords:** Fracture corridors; Hypogene karst conduits; Salitre formation; Carbonate
35 reservoir.

36

37 **1. Introduction**

38 Fractured and karstified carbonate rocks form significant hydrocarbon and
39 groundwater reservoirs (Xu et al., 2017). Karst systems are formed where the
40 dissolution of these rocks by the aqueous fluid is the dominant process (De Waele et
41 al., 2009). Karst features are mainly controlled by structural heterogeneities such as
42 bedding planes, faults and fractures, which affect fluid flow by providing preferential
43 pathways for geofluids with the development of secondary porosity (e.g., Balsamo et
44 al., 2016; Ennes-Silva et al., 2016, and references therein). This may influence the
45 production and exploitation of oil reservoirs (Ogata et al., 2012; Frumkin, 2013;
46 Klimchouk et al., 2017).

47

48 An accurate characterization of karst systems, common in carbonate reservoirs,
49 requires special attention given that this type of reservoir represents 60% of the
50 world's oil and 40% of the world's gas reserves (Montaron, 2008) and 25% of the

51 water supply, up to 50% or more in some countries (Ford and Williams 2007).
52 Therefore, they have high economic and social importance. Understanding the time-
53 space evolution, geometry and size of karst porosity is fundamental in modeling and
54 predicting fluid flow in carbonate aquifers and oil reservoirs (Popov et al., 2007; Agar
55 and Geiger, 2015; Gholpouir et al., 2016; Xu et al., 2017; Lyu et al., 2020).

56

57 The main mechanisms controlling karst distribution are chemical processes
58 (oxidation of sulfides, and/or hypogenic biogenic CO₂), hydrothermalism, regional
59 flow and regional and local structural control (Auler and Smart, 2003; De Waele et
60 al., 2009; Ennes-Silva et al., 2016). Dissolution of carbonate rocks can occur by
61 fluids enriched in CO₂ coming from the surface (epigenic karst, e.g., Audra and
62 Palmer, 2011) or when ascending flow brings thermal CO₂-rich water (Dublyansky,
63 2012) or sulfidic fluids (Palmer and Hill, 2019). Fluids can also acquire their
64 dissolutional aggressivity by mixing processes (for example, in coastal areas,
65 Mylroie, 2012), or by localized oxidation of sulfides (e.g., pyrite) (Auler and Smart,
66 2003; Tisato et al., 2012a).

67

68 Folds may concentrate the highest strain in the fold hinge zone (Cosgrove, 2015),
69 where fractures and fracture corridors occur. The term fracture corridor will be used
70 to describe persistent subparallel fractures with consistent continuity (Ogata et al.,
71 2014). These fractures often directly influence the fluid flow in the reservoirs and
72 aquifers (Odling et al., 1999; Bagni et al., 2020).

73

74 The presence of karstified zones can cause problems such as loss of fluid circulation
75 and well collapse in the exploited oil field (Xu et al., 2017). Therefore, decisions

76 about reservoir prospecting and exploration are carried out amid many uncertainties
77 arising from a poor understanding of the properties of these systems (Ogata et al.,
78 2014; Klimchouk et al., 2016).

79

80 However, karst can also significantly enhance fluid flow in carbonate reservoirs
81 (Pantou, 2014). Karst flow pathways may form very high-permeability zones (super-K
82 zones), characterizing an important factor assessed in oil reservoirs (Questiaux et al.,
83 2010; Ogata et al., 2012, 2014), which can connect different mechanical units and
84 compartmentalize reservoirs in different stratigraphic levels (Questiaux et al., 2010;
85 Bagni et al., 2020) and therefore optimize the oil production.

86

87 Even with the recent advances in knowledge about karst and fractures connecting
88 different parts of rock masses (Pollard and Aydin, 1988; Matthäi and Belayneh, 2004;
89 Narasimhan, 2005), several parameters such as karst evolution, geometry, structural
90 control, and their influence on carbonate reservoirs have not been fully clarified
91 through conventional exploration techniques such as seismic surveys because they
92 are too small to be detected by seismic surveys or wells.

93

94 Major karst features can be observed at the seismic scale but, due to the limitation of
95 the seismic resolution (>10 m), minor features often remain undetected (Tian et al.,
96 2017). Several geoscientists have been applying new methodologies combined with
97 seismic data to optimize the prediction of karst, such as thin section analyses and
98 C/O isotope ratios of core samples, borehole images, 3D delineation methods (Tian
99 et al., 2015 and references therein), and well-seismic inversion (Zhao et al., 2015).

100 However, despite the appreciable progress, major karst flowpaths are still often
101 overlooked in conventional seismic lines.

102

103 Hence, the use of carbonate outcrop analogues (Guerriero et al., 2010, 2011; Santos
104 et al., 2015; Giuffrida et al., 2019; La Bruna et al., 2018, 2020; Balsamo et al., 2020)
105 could provide insights about these systems to minimize errors in development and
106 production in carbonate reservoirs and allow for more reliable reservoir or aquifer
107 reconstruction. To fill the aforementioned gaps, analogue outcrop studies can be
108 used in some cases to supply the additional data required for the inter-well fracture
109 property population (de Jossineau and Aydin, 2007; Panza et al., 2015).

110

111 This contribution focuses on the reconstruction of paleo-flow pathways below seismic
112 resolution (less than 10 m) by analyzing subseismic-scale fractures and folds in four
113 hypogenic karst systems developed within the carbonate succession of the Salitre
114 Formation, (Fig. 1 a, b), an analogue of fractured and karstified reservoirs within the
115 São Francisco Craton (SFC, Almeida et al., 2000) and adjacent areas.

116

117 In this study, we employed a multiscale and multidisciplinary approach involving
118 petrographic characterization, qualitative and quantitative structural analysis, and high-
119 resolution Light Detection and Ranging (LiDAR) imagery. LiDAR analysis was
120 performed to provide first-order predictions on the occurrence and geometry of karst
121 features and to better understand the relationship between diffuse or localized
122 deformation on the development of flow pathways. We present a first-order prediction
123 of the occurrence and geometrical attributes in karstified carbonate rocks to shed new

124 light on the role played by both diffuse and localized deformation on the development
125 of flow pathways.

126 'Figure 1 here'

127 **2. Geological and speleological settings**

128 The SFC (Almeida et al., 2000) (Fig. 1 a) corresponds to the western portion of a large
129 cratonic area together with the Congo Craton in Africa, which were segmented during
130 the Pangea breakup and opening of the South Atlantic Ocean in the Late Jurassic and
131 Early Cretaceous (Alkmim and Martins-Neto, 2012; Cazarin et al., 2019). The most
132 recent part of the SFC is composed of Meso- and Neoproterozoic sedimentary units:
133 the Una Group, which overlaps both Paleoproterozoic and Archean basement units.
134 Within the SFC, the Irecê and Una-Utinga basins were formed by rifting that occurred
135 during the fragmentation of the Rodinia supercontinent (c. 950 – 600 Ma) (Condie,
136 2002; Guimarães et al., 2011). The presence of normal faults in the Una Group
137 indicates that the extensional tectonic regime continued until the sedimentation of
138 these Neoproterozoic basins (Misi and Veizer, 1998; Guimarães et al., 2011). A later
139 deformation stage occurred during the Brasiliano orogeny (~ 650 – 500 Ma) (Misi and
140 Veizer, 1998). Two main phases of deformation, marked respectively by folds and
141 thrusts that strike NNE-SSW and E-W, are related to collisional events on the margin
142 of the SFC during the Brasiliano orogeny (Guimarães et al., 2011; Ennes-Silva et al.,
143 2016; Boersma et al., 2019).

144

145 The Salitre Formation represents an excellent natural laboratory to investigate the
146 relationship between karst systems and fractured carbonate reservoirs. This unit
147 occurs at the top of the Una Group, is approximately 500-m thick, and is mostly
148 composed of carbonate units (Misi and Veizer, 1998). The Salitre Formation hosts

149 hundreds of caves, including the longest cave systems in South America, with a
150 combined length of over 140 km of passages (Auler et al., 2017). Most caves were
151 developed in deep-seated confined conditions, formed by a combination of rising flow
152 that migrated upward through the basal units and then spread laterally (Klimchouk et
153 al., 2016) and oxidation of sulfide-rich beds in shallow aquifers (Auler and Smart,
154 2003). Bertotti et al. (2020) highlighted the local development of caves formed along
155 strike-slip faults, displaying clear evidence of the interaction between silica-rich fluids
156 and carbonate rocks during cave formation that is rarely observed in other settings
157 worldwide.

158

159 In almost all cave systems, folds and related fractures control the planimetric
160 development of the passages (Auler and Smart, 2003). The development of a huge
161 number of caves in the Salitre Formation mostly occurred along fold hinges (Ennes-
162 Silva et al., 2016; Boersma et al., 2019). The deformation features visible in the caves
163 include stylolites, open mode fractures (joints and veins), stratabound (SB, confined
164 within mechanical unit) and non strata-bound (NSB, smaller and greater than the
165 mechanical unit) fractures and conjugate shear fractures (Ennes-Silva et al., 2016;
166 Boersma et al., 2019, Balsamo, et al., 2020).

167

168 The stratigraphic features of the caves in the northern part of the Irecê basin were
169 described by Cazarin et al. (2019). They identified five units from the bottom to the top:
170 (1) grainstones with cross-bedded stratification, (2) fine grainstones with chert nodules,
171 (3) microbial carbonates, (4) fine siliciclastic layers and marls, and (5) crystalline
172 grainstone interfingering with chert layers. The compositional difference in these units
173 is related to the variable degrees of diagenesis and provides these rocks different

174 petrophysical properties. Some units concentrate fluid flow whereas others act as
175 sealing units, preventing the fluid flow and intensifying the dissolution in the underlying
176 layers (Cazarin et al., 2019; Balsamo et al., 2020).

177

178 **3. Methods**

179 In this study, four caves were selected, known by local name: the loiô, Torrinha,
180 Lapinha, and Paixão (Fig. 1b). All caves are interpreted as displaying features
181 associated with confined flow/hypogenic conditions (Auler, 1999), although epigenic
182 features (and earlier) may occur. Data integration allowed for clarifying the relationship
183 between the physical properties of the host rocks and both fracturing and karstification
184 processes. We describe the above-mentioned analyses in the following sections.

185

186 *3.1 Petrographic and lithostratigraphic analyses*

187 The laboratory work included the petrographic analysis of 22 thin oriented sections
188 obtained from samples collected in the caves. The petrographic analysis was carried
189 out using a Leica DMLP optical microscope under planar and cross-polarized lights.
190 Based on their texture, carbonate rocks were described according to Dunham (1962).
191 This analysis allowed for us to define the composition, sedimentary facies, and texture
192 of the karstified carbonates. Four stratigraphic columns, one for each cave, were
193 reconstructed and sampled in key sectors. This approach was employed to understand
194 which units had the highest degree of dissolution (more dissolved) based on the
195 distribution of facies and mineral composition.

196

197 *3.2 Structural analysis*

198 Deformation features in the caves of the Salitre Formation were measured and sorted
199 into different types: mode I fractures (joints and veins), bed-parallel stylolites,
200 conjugate shear fractures (i.e, minor faults), and fold hinges. Joints and veins include
201 both SB and NSB structures. Bedding attitude and dip variations were also measured
202 systematically. Detailed qualitative and quantitative structural analyses were carried
203 out at each site studied. The qualitative analysis aimed at deciphering the nature,
204 kinematics, relative timing, and attitude of individual features affecting the carbonate
205 rock multilayers.

206

207 Moreover scanline analyses were performed (Marrett et al., 1999; Ortega et al., 2006;
208 Miranda et al., 2014; Giuffrida et al., 2019; Pontes et al., 2019). In total, 603 fractures
209 were measured, interpreted and analyzed with stereonet software (Allmendinger et al.,
210 2011). These analyses were performed along the sub-vertical walls at the external
211 portion of cave entrances. At each site analyzed, the 5-m-long parallel-to-bedding
212 scanlines were located orthogonally to the main fracture striking-sets (N-S and E-W
213 direction) to be as representative as possible of all the structural features present. For
214 each fracture, we measured the following parameters: attitude, height, distance from
215 the origin of the scanline, type (joint, shear joint, fault), aperture and infill (if present).
216 The aperture was measured using a comparator developed by Ortega et al. (2006).
217 The real spacing between fractures was calculated with trigonometric equations using
218 the azimuthal angle formed by the scanline plunge/dip and the main strike/dip of each
219 set (Terzaghi, 1965). The Coefficient of variation (Cv) was calculated; it consists of the
220 ratio between the σ_1 standard deviation and the mean value of fracture spacing of
221 individual fracture sets (Zambrano et al., 2016; Giuffrida et al., 2019). Furthermore, the
222 best-fit equations were calculated for the recognized individual fracture striking-sets.

223 This distinction among fracture striking-sets was determined by plotting the mean
224 fracture spacing and their cumulative number, cn , in bi-logarithmic plots (Gillespie et
225 al., 1993; Railsback, 1998; Odonne et al., 2007).

226

227 3.3 LiDAR survey

228 The caving club “*Grupo Bambui de Pesquisas Espeológicas*” provided the cave maps
229 with topographic data from the caves. Using these maps, it was possible to formulate
230 data acquisition strategies for LiDAR, boundary outlines, and the structural maps of
231 caves. The purpose of this technique was to understand the karst geometry and the
232 relation with the fracture pattern. We carried out scanning with a terrestrial LiDAR
233 system (TLS) using a Leica Scanstation P40 scanner from ViGeA (Reggio Emilia, Italy)
234 and a mobile LiDAR system (MLS), a ZEB-Revo GeoSLAM scanner. The MLS shows
235 better results for the cave morphology and irregularities in the passages. In addition,
236 the user could go through complex cave passages with the MLS during the acquisition
237 of the 3D point clouds without changing stations, which provided quick and better
238 results to identify the cave morphology. The TLS can provide more accuracy and
239 precision due to the series of additional sensors such as an inclinometer, an electronic
240 compass and a dual-axis compensator (Fabbri et al., 2017; De Waele et al., 2018)
241 LiDAR scanning can reveal the importance of fractures in karstification (Jacquemyn et
242 al., 2012). At least 35 M points were acquired for each cave studied.

243

244 We processed the point clouds with the open-source software Cloud Compare using
245 the raw file from the LiDAR data. Cloud Compare offers several tools to improve the
246 analysis of cave morphology (Fabbri et al., 2017; De Waele et al., 2018) and geometry.
247 MLS data were loaded to plot the intensity values of the scalar field using grayscale.

248 For a good visualization of the structural features, we used the “Eye-dome Lighting”
249 filter. We created 3D model slices of several parts to visualize the geometry around
250 and inside the cave using the “Cross Section” tool. Approximately 1.4 km of cave
251 passages were surveyed, approximately 350 m in the loiô cave, 500 m in the Torrinha
252 cave, 240 m in the Lapinha cave, and 200 m in the Paixão cave.

253

254 **4. Results**

255 *4.1 Lithostratigraphy of cave systems*

256 In the area of the four investigated caves, the carbonate rocks of the Salitre Formation
257 are arranged in millimeter- to centimeter-thick tabular layers. Stratigraphic analysis
258 indicates three main lithologies, from the base to the top: (a) microbial carbonates, (b)
259 microbial carbonates with intercalations of siltstone levels, and (c) sedimentary breccia
260 (Fig. 2a).

261

'Figure 2 here'

262 The carbonate layers that are microbial carbonate display chert nodules or dark *boudin*
263 concretions in some portions (Fig. 2a.). The thin sections analysis indicates that the
264 texture of these carbonate layers are mudstones affected by an intensive process of
265 dolomitization. The primary porosity of lithologies that compose the Salitre Formation
266 was reduced mostly by mesodiagenesis cementation (Cazarin et al., 2019). The
267 secondary porosity was mostly represented by fractures. The mudstone interval shows
268 a smaller grain size, with a particle-size distribution classified as silt, with frequent chert
269 nodules and pyrite present (Fig. 2 b, c).

270

271 The microbial carbonate with siltstone levels is a mudstone (Fig. 2 d, e) affected by
272 dolomitization and characterized by detritic minerals that correspond to 10-20% of their

273 composition. The sedimentary breccia (Fig. 2 f, g) corresponds to grainstone
274 characterized by a coarse grain size (sands). Specific layers display less significant
275 dissolution compared with others, forming high relief zones (prominent layers) that vary
276 according to rock texture and composition (Fig. 3). Usually, the mudstone with siltstone
277 levels and the grainstone are more prominent in relief inside the caves than the
278 mudstone layers (Fig. 3). Occasionally within the mudstone layers, we identified darker
279 intercalations composed of organic material and/or pyrite (Fig. 2 c), which indicate a
280 reducing environment.

281 'Figure 3 here'

282 *4.2 Structural data*

283 We divided this topic into quantitative and qualitative approaches. The qualitative
284 approach included detailed structural mapping and LiDAR imaging analysis to identify
285 the relationship between the fracture sets and principal fracture zones, as well as the
286 characterization of the cave features. A quantitative field fracture analysis was
287 performed along the surveyed carbonate rock walls to distinguish the diffuse
288 deformation from the fold-fault related deformation and determine their influence on
289 the cave's nucleation and development.

290

291 *4.2.1 General cave features*

292 The qualitative structural analysis based on field observations, LiDAR imaging, and
293 structural measurements was performed within the caves and along the external sub-
294 vertical walls that surround the cave entrances. We documented fractures (joints,
295 veins, sheared joints, and sheared veins), bed-parallel stylolites, sedimentary bedding,
296 and fold hinges. Commonly, bed-parallel stylolites are located at the bed interfaces
297 within mm-thick, continuous, clay-rich marl levels. Less often, they are present within

298 individual carbonate beds. Open-mode fractures may display hackles and ribs and thus
299 were identified as joints. In some cases, a millimeter-to-centimeter offset of
300 depositional surfaces was observed across them and thus we considered the above
301 features to be sheared joints. Some of the cave passages exhibit an alignment of
302 speleothems located in the central part of the cave roofs. These speleothems are
303 mainly associated with several fracture zones parallel to the cave passages and
304 running along the central part of the cave roofs (Fig. 4 a). The cave passages are
305 arranged in a linear or maze pattern, with rectilinear sub-horizontal passages
306 developed parallel to fractures in an orthogonal pattern (Fig. 4 a, b). High dissolution
307 zones occur in the middle portion of the cave passages (Fig. 4 c). In general, cave
308 galleries could be divided into major chambers ~ 10-m high and smaller conduits up to
309 2.5-m high that link the major chambers. The preferred direction of the cave passages
310 coincides with the main persistent N-S- and E-W-striking fracture zones.

311 'Figure 4 here'

312 Fractures may be confined within individual carbonate beds as SB, usually observed
313 away from the main dissolution zones, or as NSB where they crosscut one or several
314 beds, usually related to main dissolution zones. Both SB and NSB fractures are much
315 more evident along the external portion of the caves where the dissolution and
316 mineralization processes do not entirely erase or overprint them (Fig. 5 a, b). The SB
317 and NSB fractures are not necessarily parallel (Fig. 5 c). However, the high dissolution
318 zones are parallel to the main persistent NSB fractures.

319 'Figure 5 here'

320 Two main fracture sets were observed in the study sites, striking N-S and E-W;
321 systematically, the E-W fractures terminate against the N-S ones, which indicates that
322 the latter are older than the former (Fig. 6 a). Bed-parallel stylolites are common
323 throughout the analyzed sites, at the surface and inside the caves. We also

324 documented bed-perpendicular folded veins (Fig. 6 b) and several high-angle normal
325 faults characterized by extensional or oblique kinematics (Fig. 6 c and d). Usually,
326 these structures are composed of several discontinuous slip surfaces; the
327 abutting/crosscutting relationships (Fig. 6 d) among the fracture sets are consistent
328 with their hierarchical formation and subsequent shearing of joint sets sub-parallel to
329 the main slip surfaces (Davatzes and Aydin, 2003; Myers and Aydin, 2004).

330 'Figure 6 here'

331 *4.2.2 Identification of fold hinges and fracture sets*

332 Two major gentle folds occur in the loiô cave (Fig. 7 a, b, c, d). These antiforms display
333 a N-S fold axis, which is parallel to the main cave passage and the main
334 fracture/dissolution zones (Fig. 7 e, f). Along the cave passages, the bed surfaces
335 display a dip of approximately 10° toward the west (along the western cave wall) and
336 10° toward the east (along the eastern wall, Fig. 7 c, d, g).

337 'Figure 7 here'

338 We performed LiDAR surveys in all the caves. In the Lapinha cave (Fig. 8 a) the LiDAR
339 survey was integrated with detailed structural analysis at 13 sites (Fig. 8 b). This cave
340 is marked by the presence of two orthogonal, bed-perpendicular fracture sets that
341 strike ~ N-S and E-W (Fig. 8 c). Along the ~ N-S passages, the bed surfaces show dip
342 ranging from 3° to 15° toward the east and west. E-W cave passages show a bedding
343 dip from 5° to 10° toward the north and south (Fig. 8 d and e). The main
344 fracture/dissolution zones are parallel to the documented fold hinges and concentrated
345 along the central portion of the cave ceilings (Fig. 8 c, d). Furthermore, the LiDAR data
346 analysis allowed for us to highlight and measure the fold wavelengths in the Lapinha
347 cave. E-W and N-S folds display an almost equidistant wavelength of ca 30 m (Fig. 8
348 e).

349 'Figure 8 here'

350 The high-resolution imaging provided by the MLS survey in a maze portion of the
351 Torrinha cave provides a consistent representative model of the geometry of the cave
352 passage (Fig. 9 a, b) and allowed for us to determine that the karstification processes
353 followed the direction of fold hinges. The main geometric pattern observed for the cave
354 passages could be associated with an ellipsoid with a major axis in a horizontal or
355 vertical position (Figs. 9 b, c, d). The processes of dissolution are more developed near
356 or at the fracture/fault intersection, as highlighted in the 3D model of the Paixão cave
357 (Fig. 9 e) and Fig. 4 b.

358 'Figure 9 here'

359 The studied mazes in Torrinha cave displays a similar structure to the Lapinha cave,
360 characterized by an orthogonal pattern of the cave passages. This geometry is
361 highlighted by the LiDAR survey carried out in the southeastern part of the cave (Fig.
362 10 a). Along this portion, the cave is affected by folds showing both N-S and E-W hinge
363 directions (Fig. 10 b, c). The bedding dip ranges from 8° to 15° , usually in opposite
364 directions, forming gentle folds (Fig. 10 c, d). The E-W passages usually terminate
365 against the N-S structures, which are more persistent. A NW-SE strike-slip fault with a
366 dextral kinematic (Fig. 10 c) causing a displacement of N-S fold hinges was observed.
367 The detachment of carbonate layers indicates a compressive component (Fig. 10 e).

368 'Figure 10 here'

369 The Paixão cave is characterized by orthogonal cave passages and related anticlines
370 (Fig. 11 a) where these passages display an *en echelon* pattern associated with
371 several *en echelon* fold hinges (Fig. 11 b, c). The bedding dip ranges from 4° to 18°
372 along the cave walls (Fig. 11d). One of the main cave passages is associated with a
373 single fault zone (Fig. 11 e) showing high displacement (HD) in the central part,
374 observed in the LiDAR digital model (Fig. 11 g). Along this fault zone, we also identified
375 and characterized several dip-slip faults (Figs. 11 g, h).

376

'Figure 11 here'

377 *4.2.3 Background and clustered fractures*

378 The quantitative structural analysis based on the scanline methodology was performed
379 along the external vertical walls. The scanline measurements were taken to decipher
380 the nature, orientation, geometry, dimension, and multi-scale properties of background
381 and clustered fractures. The values of the exponential distribution, power law
382 distribution and C_v are summarized in table 1.

383

'Table 1 here'

384 The N-S-striking set shows C_v values higher than 1 for the loiô (Fig. 12 a), Lapinha
385 (Fig. 13 a), and Torrinha sites (Fig. 14 a), and values lower than 1 for the Paixão site
386 (Table 1). The same results were observed for the NNW-SSE-striking set. The C_v
387 values of the NW-SE-striking set are close to 2 in the loiô site; they range from 0.8 and
388 1.7 in the Torrinha site and they from 0.29 to 0.99 in the Paixão site. In the loiô site,
389 the E-W- and NE-SW-striking sets show C_v values lower than 1. However, in the
390 Torrinha and Lapinha sites, which exhibit caves with maze geometries, the E-W- and
391 NE-SW-striking sets exhibit C_v values higher than 1, reaching 2.26 at scanline 1 of the
392 set NE-SW (Table 1). Only in the Paixão site, all striking-sets (Fig. 15 a) present C_v
393 values lower than 1 for all scanlines.

394

'Figure 12 here'

395

'Figure 13 here'

396 The multi-scale spacing distribution computed for the SB and NSB fracture sets (Figs.
397 12 b, 13 b, 14 b, 15 a) is presented in Figures 12 c, 13 c, 14 c, and 15 b, in which the
398 fracture spacing is plotted in a log-log space versus as a cumulative number. In the
399 loiô site, the N-S-striking set (Fig. 12 b, 13 b, 14 b, 15 a) shows a power-law distribution
400 (Fig. 12 c); the same occurs at scanline 3 in the Torrinha site (Fig. 14 c). All other N-S
401 striking-set scanlines show an exponential distribution in the Lapinha and Paixão sites

402 (Figs. 13 c, 15 b). The NNW-SSE- and NW-SE-striking sets present the same behavior
403 as the N-S-striking set. In the Ioiô and Torrinha sites, the E-W-striking set shows an
404 exponential distribution. In the Lapinha site, the E-W-striking set presents both an
405 exponential and power-law distribution (Fig. 13 c). In the Paixão cave, all measured
406 striking-sets, N-S, NW-SE, and NNW-SSE, exhibit an exponential distribution (Fig. 15
407 b). The NE-SW-striking set in the Ioiô and Lapinha sites show a power-law distribution
408 (table 1). In all cave sites, the clustered fracture sets (fracture corridors) exhibit the
409 same trend as that in the main cave passage.

410 'Figure 14 here'

411 'Figure 15 here'

412 **5. Discussion**

413 *5.1 The origin and evolution of fracture corridors and flow pathways in multiple-* 414 *direction fold hinges*

415 The prediction of flow pathways that connect different parts of reservoirs may provide
416 useful information to interpret fluid flow at a subseismic scale and could optimize oil
417 field development planning. The evolution of subseismic flow pathways in multiple-
418 direction fold hinges may be explained in four stages: background deformation, E-W
419 compression, N-S compression, and karst development. Quantitative analysis
420 performed for our study sites allowed for discriminating the fracture sets associated
421 with a previous stress field related to burial (background deformation) from the fracture
422 sets related to the fold-fault events that could play a key role in fluid migration
423 processes.

424

425 Focusing on the fractures that have been analyzed, the first stage (background
426 deformation) is characterized by cross-orthogonal bed perpendicular joints related to
427 diffuse deformation in different striking sets. Fracture sets related to diffuse

428 deformation and the bed-parallel stylolites could be associated with the overburden of
429 the Salitre Formation (Figure 16 a, Ennes Silva et al., 2016). The bed-parallel stylolites
430 occur inside the stratigraphic layers as well as in the interface between layers. The
431 burial deformation is the first stage marked by the aforementioned fracture sets and
432 bed-parallel stylolites. Permutation of the sub-horizontal σ_2 and σ_3 principal stress
433 likely took place during burial diagenesis of the studied carbonate succession allowing
434 for the formation of both N-S and E-W fracture sets (Bai et al., 2002). The joint sets
435 are mainly characterized by a negative exponential, multi-scale spacing distribution,
436 which is distinctive of a diffuse deformation (Ortega et al., 2006). Moreover, the range
437 of C_v variations is consistent with randomly distributed fractures (Gillespie et al., 1993).

438

439 The second stage of evolution of flow pathways is related to E-W compression (Fig.
440 16 b). This tectonic compression occurred during the major folding event, N-S
441 shortening, related to the Brasiliano orogeny (Ennes Silva et al., 2016), which
442 developed gentle fold sets that display fold hinges mainly striking N-S (Fig. 7 d, e).
443 During this second stage of deformation, nucleation and development of the NW-SE,
444 NE-SW, NNE-SSW and NNW-SSE-striking fracture sets occurred. These structural
445 elements were associated with the shearing of the pre-existing N-S fractures and the
446 development of incipient faults (Figs. 6 c, 6 d, 11 e, 11 f, 11 g, 11 h). These fracture
447 sets were described by a power-law distribution, typical of clustered deformation. C_v
448 values usually range from 1.03 to 2.2 and thus these fracture sets are ascribed to a
449 folding event or a mature stage of faulting (de Jossineau and Aydin, 2007).

450

451 The third stage is the development of folds displaying a basin-dome configuration
452 (Ramsay, 1967) due to N-S shortening (Fig. 16 c). E-W fold hinges and NW-SE strike-

453 slip faults (Fig. 10 c, e) characterize this tectonic compression. A displacement of the
454 N-S fold hinge reinforces that the N-S trends predate the development of this strike-
455 slip fault. These two contractional phases were also documented by previous research
456 conducted by Cruz and Alkmim (2006), Guimarães et al. (2011), Ennes-Silva et al.
457 2016, Klimchouk et al. (2016), D'Angelo et al. (2019) and Balsamo et al. (2020). Ennes-
458 Silva et al. (2016) proposed the generation of a superposed fold pattern initiated by
459 NW-SE-oriented compression, which initially formed NNE-SSW-oriented joints and E-
460 W folds and then E-W-oriented joints and N-S folds associated with a thrust in the
461 northern portion of the Salitre Formation. In our study in the southern portion of the
462 Salitre Formation, we suggest that the first contractional phase is evidenced by E-W
463 compression that originated N-S and NNE-SSW fold hinges and N-S-striking fractures
464 that are more pervasive than the E-W fold hinges and E-W-striking fractures. This
465 sequence of contractional events, with E-W structures younger than N-S, was also
466 documented by D'Angelo et al. (2019). E-W-oriented fractures abut against N-S-
467 striking fractures, supporting this interpretation.

468

469 In the proposed generation of superposed folds, the development of fracture corridors
470 predates the entry of fluid into the system, which represents the last stage on the
471 development of flow pathways. The same brittle mechanism with contractional control
472 was documented by Agosta and Aydin (2006), La Bruna et al., (2017), and Mazzoli et
473 al. (2014) for tight carbonates cropping out in central and southern Italy, which were
474 interpreted as a poly-phasic tectonic activity. From the cross-cutting and abutting
475 relationship, it is possible to deduce that the E-W-striking fractures developed later
476 than the N-S-striking fractures (Fig. 6 a; 10 c), Moreover, along the intersection or
477 fracture termination zones, the karstification process is enhanced (Fig 4 b, 9 d). Bed-

478 parallel stylolites and bed-perpendicular folded veins indicate the variation in the stress
479 fields that affected these carbonate rocks (Fig. 6 b). Based on the crosscutting
480 relationship, it is possible to deduce that the bed-parallel stylolites predate bed-
481 perpendicular folded veins.

482

483 After the development of both fracture sets and the extension localized along fold
484 hinges, rising fluid flow interacted with the surrounding rocks (Figure 16 d). Due to the
485 very low primary porosity of the carbonate rocks, ranging from 0% to 7% (Cazarin et
486 al., 2019), the fractures acted as preferential fluid pathways. NSB fracture corridors
487 localized along fold hinges increased permeability and connectivity (Fig. 3, 4 a, 4 b)
488 (Bagni et al., 2020). The fluid-rock interaction may directly affect the fluid flow and
489 storage (Evans and Fischer, 2012), making high dissolution zones (super-K zones)
490 (Figs. 4 c, 7 e, 7 f). The high dissolution/karstification rate following fracture corridors
491 is evidenced by the cave pattern, forming a typical hypogene maze, and the lack of the
492 downward carving vadose infiltration passages typical of epigenic cave systems. The
493 alignment of speleothems following these fractures highlights the presence of the
494 structural fluid flow pathways, which are still exploited by present epigenic infiltrating
495 waters (Fig. 3, 4 a, Kim and Sanderson, 2010).

496

497 The fourth stage of development of karst conduits is related to lithologic/stratigraphic
498 control. Even with the development of cave passages along fold hinges, differential
499 degrees of karstification (Fig. 3) in the observed lithologies, based on the cross-section
500 morphology of the cave, indicate that the development of the karst in carbonate rocks
501 is also related to their composition. Field and laboratory analyses suggest that the
502 composition of these rocks definitely influenced can influence the karst development

503 (de Melo et al., 2015; Baiyegunhi et al., 2017). Carbonate rocks that have a finer grain
504 size are more readily dissolved (Fig. 2 c), which would have focused the dissolution
505 process and the fluid flow. Moreover, the presence of pyrite (Worthington and Ford,
506 1995; Palmer, 2016) (Fig. 2 c) may have contributed to an increase in the karstification
507 process by H₂S oxidation (Auler and Smart, 2003; Tisato et al., 2012; D'Angeli et al.,
508 2019). The primary porosity of these rocks is very low, so it is the secondary porosity
509 (i.e., fractures, that are strongly related to the rock composition, Balsamo et al., 2020)
510 that guides karstification (Cazarin et al., 2019). The layers characterized by lower
511 dissolution rates correspond to grainstone with clasts and a coarser grain size (Fig. 2
512 f, g) and mudstone interspersed with siltstone levels with high detritic mineral content
513 (15-20%), mainly quartz grains (Fig. 2 d, e). The compositional variation in the wall
514 rocks leads to the present-day visible karst geometry.

515 'Figure 16 here'

516 *5.2 Development of karst conduits according to the deformation stages*

517 The development of karst conduits in the Salitre Formation's carbonate units follows
518 the structural and compositional controls mentioned above, but each cave has unique
519 characteristics. We performed a statistical analysis to provide a useful model for
520 comparison of the fracture sets that influenced the development of karst conduits in
521 each cave. For the loiô cave (Fig. 7), the N-S-, NW-SE-, and NE-SW-striking sets show
522 a power-law distribution rather than an exponential distribution, and they could be
523 associated with a localized deformation (fold-fault related, Ortega et al., 2006). The Cv
524 of these fracture sets is higher than 1 whereas the N-S sets display Cv values greater
525 than 1.9. Therefore, we affirm that the N-S-, NW-SE-, and NE-SW-striking sets are
526 clustered, and could be related to a folding process. The E-W-striking fracture set
527 displays an exponential distribution and lower Cv of 0.85 and 0.75, which indicate a

528 diffuse deformation. As the N-S-, NW-SE-, NNW-SSE-, and NE-SW-striking sets show
529 a power-law distribution in the Ioiô site (Table 1), we conclude that the development of
530 the Ioiô cave passages is related to fold-related fractures concentrated along fold
531 hinges.

532

533 In the Lapinha cave (Fig. 8), all fracture sets (NE-SW, N-S, WNW-ESE, and E-W) show
534 Cv values greater than 1, which indicates a clustered deformation (Gillespie et al.,
535 1993; de Jossineau and Aydin, 2007). Only the NE-SW-striking set, with a Cv value
536 of 2.26, shows a power-law distribution (Table 1). The range of Cv variations is
537 consistent with both even-spaced and clustered fracture distributions in the carbonates
538 (Gillespie et al., 1993). The Cv higher than 1 and variation in the power-law and
539 exponential distributions implies that multiple-stage jointing occurred during the burial
540 and subsequent evolution of the Salitre Formation.

541

542 The striking sets of the Torrinha cave (N-S, NNW-SSE, NW-SE and E-W, Fig. 10 b)
543 show a similar behavior, with Cv values higher than 1, but only the N-S striking set
544 shows more power-law distribution than exponential distribution, which is related to the
545 aforementioned multiple-stage jointing. We suggest that mostly N-S-oriented joints
546 were formed during the fold event, and NNW-SSE-, NW-SE- and E-W-oriented striking
547 sets may be formed during the burial and may have reactivated during a tangential
548 stress regime.

549

550 In the Paixão cave (Fig. 11 a), the N-S-, NW-SE- and NNW-SSE-striking sets (Figure
551 15 a) show a better correlation with the exponential distribution than a power-law
552 distribution. The Cv of these sets is lower than 1, from 0.34 to 0.88. Based on these

553 values and the good correlation with an exponential distribution, we suggest that these
554 fractures do not originate during the folding process. These striking sets may have
555 formed during the burial history of the Salitre Formation, and may have reactivated
556 during the folding event.

557

558 Faults may form preferential flow paths and guide fluid migration (Ligtenberg, 2004;
559 Wilson et al., 2011; Ogata et al., 2012, 2014; Balsamo et al. 2019). Karst development
560 may also follow fracture corridors generated in fault damage zones (Fig. 10 e, Ogata
561 et al., 2014). The process of karstification in faults as well as in folded zones is
562 observed worldwide, for example, in the Tarim Basin where these areas represent
563 ideal targets for oil (Xu et al., 2017). In the Paixão cave, it was observed that cave
564 passages developed following an *en echelon* pattern (Fig. 10 b, c). In the central
565 portion of the fault zone, which has the highest deformation and displacement rates
566 (Ogata et al., 2014), a subvertical master fault was observed (Fig. 10 e, f) and a
567 transtensive structure developed at the edge of the fault zone (Fig. 10 g, h). This allows
568 for us to affirm that cave passages follow both anticline fold hinges and fault zones.

569

570 *5.3 Implications for fluid flow in carbonate units*

571 Tectonic structures greatly impact the fluid flow in carbonate units (Goldscheider, 2005;
572 Dewever et al., 2010; Pantou, 2014; Agosta et al., 2015; Cosgrove, 2015; Ennes-Silva
573 et al., 2016; Wang et al., 2017; Boersma et al., 2019; Balsamo et al., 2020). Structures
574 such as fracture corridors often form preferential zones for fluid flow (Ogata et al., 2014;
575 Souque et al., 2019), but the location of their occurrence is an enormous challenge for
576 the oil industry because they are barely visible at a seismic resolution (Lamarche et
577 al., 2018). Understanding the key factors in their formation, distribution and geometry

578 may contribute to flow modeling for fractured carbonate rocks (Goldscheider, 2005)
579 and to the assessment of their impacts on the development of karstified reservoirs.

580

581 Structural data allowed for correlating diffuse and localized fold-fault-related
582 deformation with influence on the development of the hypogenic caves analyzed. This
583 information provides new insights on storage and fluid flow properties. The qualitative
584 analysis indicates that the development of the karst-conduits investigated is mainly
585 related to highly persistent fractures, usually visible along the central portion of the
586 roofs of these caves and parallel to the fold hinges (Evans and Fischer, 2012), creating
587 a high-dissolution zone (Figures 4 c, 7 e, f). This evidence was also reported and
588 documented in many other cases around the world, including the Middle East oil fields,
589 pre-salt reservoirs offshore Brazil and the Tarim Basin in China (Pollastro, 2003;
590 Menezes et al., 2016; Li et al., 2018). Li et al. (2018) highlighted that trending fractures
591 in the extensional area of faulted folds are better developed than the fractures in the
592 limb of folds improving the migration of fluids and permeability in tight sandstone
593 reservoirs. Based on our observations of high-dissolution zones located in the
594 extensional area of folds (Fig. 3; 7 c, d), it is possible to verify the same behavior in
595 carbonate rocks and carbonate reservoirs.

596

597 Fluid flow events in carbonates subdued by tectonic compression was described by
598 Warren et al. (2014), who integrated isotope data with structural surveys. Morley et al.
599 (2014) highlighted the relevance of fluid flow along fold-thrust belts in deep aquifers
600 and onshore (offshore Brunei and the Central Basin of Iran, respectively). Both works
601 highlight the importance of fractures in the migration of fluids and in the fluid-rock

602 interaction. Here, we highlight the importance of fracture corridors that, similar to
603 fractures, act as fluid pathways in fold and thrust environments.

604

605 The use of LiDAR was demonstrated to be a very useful tool for detailed cave mapping.
606 Fabbri et al. (2017b) used TLS to make detailed 3D models for morphometric
607 measurements. De Waele et al. (2018) used TLS and 3D photogrammetry to identify
608 different evolution stages of ceiling channels. Here, we applied both TLS and MLS to
609 observe the karst geometry/shape (Fig. 3, 7 e, 11 f); the MLS showed more accurate
610 results due to the ability to move the instrument through both narrow and large cave
611 passages without interrupting during acquisition.

612

613 The karst conduit shape is a response to the interaction between structural features
614 and the composition of the carbonate rocks. Structural features such as fractures and
615 fracture corridors provide space for vertical rising flow, and horizontal enlargement
616 occurs laterally along preferential carbonate layers (Klimchouk, 2009). This
617 enlargement occurs mainly in presence of mudstones with a silt grain size and pyrite
618 content that boost the carbonate dissolution by sulfide oxidation. Carbonate layers with
619 a coarse grain size and higher detritic mineral content that are absent of pyrite may
620 hinder the fluid flow and concentrate the dissolution in subjacent layers, confining the
621 ascending fluid and intensifying a horizontal fluid circulation (Klimchouk et al., 2016),
622 leading to the ellipsoidal cross-sectional shape of the karst corridors.

623

624 Hence, the development of the hypogenic caves studied following the structural control
625 (Ennes-Silva et al., 2016; Boersma et al., 2019) of the area, mainly expressed as
626 fracture corridors along orthogonal fold hinges. These fracture sets were initially

627 randomly distributed and reactivated during the folding event, with preferential N-S and
628 E-W strikes, providing localized deformation in the fold hinges generated by the
629 compression that affects the carbonate rocks (Ennes-Silva et al., 2016; Boersma et al.,
630 2019; Balsamo et al., 2020). These structural elements result from the shearing and
631 linkage of pre-existing, bed-confined N-S and E-W fractures and the formation of NW-
632 SE-, NE-SW-, NNE-SSW-, and NNW-SSE-striking tail joints, which clustered at the
633 mode-II extensional quadrants and along the Mode-III terminations of the sheared N-
634 S and E-W elements (sensu Segall and Pollard, 1983; Peacock et al., 1997; Agosta et
635 al., 2015).

636

637 The positions of fold-hinges control the fold-related N-S and E-W fractures (Awdal et
638 al., 2016) and the development of fracture corridors and karst conduits. Although
639 fracture corridors are barely visible on the subseismic scale (Lamarche et al., 2018),
640 these tectonic structures could be related to regional structures, such as fold hinges,
641 that could be observed on maximum-curvature maps (Fischer and Wilkerson, 2000),
642 for example.

643

644 **6. Conclusions**

645 The structural data and the karstification processes that affect the carbonate rocks of
646 the Salitre formation indicate that the caves develop following the main structural
647 features of the area, which is strongly influenced by fold hinges and faults. The major
648 results of this research contribute to the prediction of karst geometry and occurrence,
649 and are summarized below:

650 (a) In plan view, the cave passages are orthogonal, with a maze pattern, following the
651 structural control of the area, and are expressed as fracture corridors along fold hinges

652 and faults. The development of subseismic flow pathways is directly related to the
653 structural features that affect these rocks.

654 (b) The vertical profile of the cave passages shows an ellipsoidal shape/geometry due
655 to the textural variation that provides different karstification levels. Carbonate layers
656 that have more pyrite and less detrital minerals in their composition are more karstified
657 and can act as flow pathways. Carbonate layers with a coarser grain size and higher
658 detrital minerals content hinder the karstification. These layers often act as seals to
659 rising fluid flow.

660 (c) Fracture corridors are formed along fold hinges, even in gentle folds with a bedding
661 dip less than $\sim 10^\circ$. These fracture corridors behave like high-permeability zones (super
662 K-zones) that facilitate the vertical fluid percolation and the karstification process.
663 These fracture corridors are strongly related to fluid migration.

664 (d) Cave passages may develop during or after faulting. The secondary porosity due
665 to faulting is essential to fluid percolation. In addition, the karstification process is
666 intensified at intersections between distinct fractures sets.

667 (e) The subseismic flow pathways and karst conduits can be predicted by the accurate
668 structural analysis. Both diffuse and localized deformation, related to folds or faults,
669 may increase the process of karstification. The development of subseismic flow
670 pathways and karst conduits is intensified in a localized deformation due to the
671 clustered fractures that provide pathways and enhance the fluid flow.

672

673 **Acknowledgements**

674 This research was carried out in association with the ongoing R&D project registered
675 as ANP 20502-1, "Processos e Propriedades em Reservatórios Carbonáticos
676 Fraturados e Carstificados – POROCARSTE 3D" (UFRN / UNB / UFRJ / UFC / Shell

677 Brasil / ANP) – Porokarst – Processes and Properties in Fractured and Karstified
678 Carbonate Reservoirs, sponsored by Shell Brasil under the ANP R&D levy as
679 “Compromisso de Investimento com Pesquisa e Desenvolvimento”. Cave maps were
680 kindly provided by Grupo Bambuí de Pesquisas Espeleológicas. Cave sampling was
681 performed through SISBIO permit 63178/1. Many thanks to Alisson Jordão and Uilson
682 Teixeira for the fieldwork and Umberto Del Vecchio of ViGeA Reggio Emilia (Italy) for
683 the fieldwork and elaboration of the TLS surveys.

684

685 **References**

686 Agar, S.M., Geiger, S., 2015. Fundamental controls on fluid flow in carbonates: Current
687 workflows to emerging technologies. *Geol. Soc. Spec. Publ.* 406, 1–59.

688 <https://doi.org/10.1144/SP406.18>

689

690 Agosta, F., Aydin, A., 2006. Architecture and deformation mechanism of a basin-bounding
691 normal fault in Mesozoic platform carbonates, central Italy. *J. Struct. Geol.* 28, 1445–1467.

692 <https://doi.org/10.1016/j.jsg.2006.04.006>

693

694 Agosta, F., Wilson, C., Aydin, A., 2015. The role of mechanical stratigraphy on normal fault
695 growth across a Cretaceous carbonate multi-layer, central Texas (USA). *Ital. J. Geosci.* 134,

696 423–441. <https://doi.org/10.3301/IJG.2014.20>

697

698 Alkmim, F.F., Martins-Neto, M.A., 2012. Proterozoic first-order sedimentary sequences of
699 the São Francisco craton, eastern Brazil. *Mar. Pet. Geol.* 33, 127–139.

700 <https://doi.org/10.1016/j.marpetgeo.2011.08.011>

701

702 Allmendinger, R.W., Cardozo, N., Fisher, D.M., 2011. Structural geology algorithms: Vectors
703 and tensors, *Structural Geology Algorithms: Vectors and Tensors*.

704 <https://doi.org/10.1017/CBO9780511920202>

705

706 Almeida, F.F.M. De, Brito Neves, B.B. De, Dal Ré Carneiro, C., 2000. The origin and
707 evolution of the South American platform. *Earth Sci. Rev.* 50, 77–111.

708 [https://doi.org/10.1016/S0012-8252\(99\)00072-0](https://doi.org/10.1016/S0012-8252(99)00072-0)

709

710 Audra, P., Palmer, A.N., 2011. Structure des réseaux karstiques : Les contrôles de la
711 spéléogénèse épigène. *Geomorphol. Reli. Process. Environ.* 359–378.

712 <https://doi.org/10.4000/geomorphologie.9571>

713

714 Auler, A.S., 1999. Karst evolution and paleoclimate of eastern Brazil. University of Bristol.

715

716 Auler, A.S., Smart, P.L., 2003. The influence of bedrock-derived acidity in the development
717 of surface and underground karst: Evidence from the Precambrian carbonates of semi-arid
718 northeastern Brazil. *Earth Surf. Process. Landforms* 28, 157–168.

719 <https://doi.org/10.1002/esp.443>

720

721 Auler, A.S., Klimchouk, A., Bezerra, F.H.R., Cazarin, C.L., Ennes-Silva, R., Balsamo, F.,
722 2017. Origin and Evolution of Toca da Boa Vista and Toca da Barriguda Cave System in
723 North-eastern Brazil, in: *Hypogene Karst Regions and Caves of the World, Cave and Karst*
724 *Systems of the World*. pp. 827–840. https://doi.org/10.1007/978-3-319-53348-3_56

725

726 Awdal, A., Healy, D., Alsop, G.I., 2016. Fracture patterns and petrophysical properties of
727 carbonates undergoing regional folding: A case study from Kurdistan, N Iraq. *Mar. Pet. Geol.*
728 71, 149–167. <https://doi.org/10.1016/j.marpetgeo.2015.12.017>
729

730 Bagni, F.L., Bezerra, F.H., Balsamo, F., Maia, R.P., Dall’Aglia, M., 2020. Karst dissolution
731 along fracture corridors in an anticline hinge, Jandaíra Formation, Brazil: Implications for
732 reservoir quality. *Mar. Pet. Geol.* 115, 104249.
733 <https://doi.org/10.1016/j.marpetgeo.2020.104249>
734

735 Bai, T., Maerten, L., Gross, M.R., Aydin, A., 2002. Orthogonal cross joints: Do they imply a
736 regional stress rotation? *J. Struct. Geol.* 24, 77–88. <https://doi.org/10.1016/S0191->
737 [8141\(01\)00050-5](https://doi.org/10.1016/S0191-8141(01)00050-5)
738

739 Baiyegunhi, C., Liu, K., Gwavava, O., 2017. Diagenesis and reservoir properties of the
740 Permian Ecca Group sandstones and mudrocks in the Eastern Cape Province, South Africa.
741 *Minerals* 7(6), 88. <https://doi.org/10.3390/min7060088>
742

743 Balsamo, F., Bezerra, F.H.R., Klimchouk, A.B., Cazarin, C.L., Auler, A.S., Nogueira, F.C.,
744 Pontes, C., 2020. Influence of fracture stratigraphy on hypogene cave development and fluid
745 flow anisotropy in layered carbonates, NE Brazil. *Mar. Pet. Geol.* 114, 104207.
746 <https://doi.org/10.1016/j.marpetgeo.2019.104207>
747

748 Balsamo, F., Clemenzi, L., Storti, F., Solum, J., Taberner, C., 2019. Tectonic control on vein
749 attributes and deformation intensity in fault damage zones affecting Natih platform

750 carbonates, Jabal Qusaybah, North Oman. *Journal of Structural geology*, v. 122, pp. 38-57.

751 <https://doi.org/10.1016/j.jsg.2019.02.009>

752

753 Balsamo, F., Clemenzi, L., Storti, F., Mozafari, M., Solum, J., Swennen, R., Taberner, C.,

754 Tueckmantel, C., 2016. Anatomy and paleofluid evolution of laterally-restricted extensional

755 fault zones in the Jabal Qusaybah anticline, Salakh Arc, Oman. *Geological Society of*

756 *America Bulletin*, v. 128, p. 957–972, doi: 10.1130/B31317.1

757

758 Bertotti, G., Audra, P., Auler, A.S., Bezerra, F.H.R., de Hoop, S., Pontes, C., Prabhakaran, R.,

759 Lima, R., 2020. The Morro Vermelho Hypogenic Karst System: stratigraphy, fractures and

760 flow in a carbonate strike-slip fault zone with implications for carbonate reservoir. *Am.*

761 *Assoc. Pet. Geol. Bull.*

762

763 Boersma, Q., Prabhakaran, R., Bezerra, F.H., Bertotti, G., 2019. Linking natural fractures to

764 karst cave development: a case study combining drone imagery, a natural cave network and

765 numerical modelling. *Pet. Geosci.* 25(4), 454-469. <https://doi.org/10.1144/petgeo2018-151>

766

767 Cazarin, C.L., Bezerra, F.H.R., Borghi, L., Santos, R. V., Favoreto, J., Brod, J.A., Auler, A.S.,

768 Srivastava, N.K., 2019. The conduit-seal system of hypogene karst in Neoproterozoic

769 carbonates in northeastern Brazil. *Mar. Pet. Geol.* 101, 90–107.

770 <https://doi.org/10.1016/j.marpetgeo.2018.11.046>

771

772 Condie, K.C., 2002. The supercontinent cycle: Are there two patterns of cyclicity? *J. African*

773 *Earth Sci.* 35, 179–183. [https://doi.org/10.1016/S0899-5362\(02\)00005-2](https://doi.org/10.1016/S0899-5362(02)00005-2)

774

775 Cosgrove, J.W., 2015. The association of folds and fractures and the link between folding,
776 fracturing and fluid flow during the evolution of a fold-thrust belt: A brief review. *Geol. Soc.*
777 *Spec. Publ.* 421, 41–68. <https://doi.org/10.1144/SP421.11>
778

779 Cruz, S.C.P., Alkmim, F.F., 2006. The tectonic interaction between the Paramirim aulacogen
780 and the Araçuaí belt, São Francisco craton region, Eastern Brazil. *An. Acad. Bras. Cienc.* 78,
781 151–173. <https://doi.org/10.1590/s0001-37652006000100014>
782

783 D'Angeli, I.M., Parise, M., Vattano, M., Madonia, G., Galdenzi, S., De Waele, J., 2019.
784 Sulfuric acid caves of Italy: A review. *Geomorphology* 333, 105–122.
785 <https://doi.org/10.1016/j.geomorph.2019.02.025>
786

787 D'Angelo, T., Barbora, M. S. C., Danderfer Filho, A., 2019. Basement controls on cover
788 deformation in eastern Chapada Diamantina, northern São Francisco Craton, Brazil: Insights
789 from potential field data. *Tectonophysics* 772, 228-231.
790 <https://doi.org/10.1016/j.tecto.2019.228231>
791

792 Davatzes, N.C., Aydin, A., 2003. Overprinting faulting mechanisms in high porosity
793 sandstones of SE Utah. *J. Struct. Geol.* 25, 1795–1813. [https://doi.org/10.1016/S0191-](https://doi.org/10.1016/S0191-8141(03)00043-9)
794 [8141\(03\)00043-9](https://doi.org/10.1016/S0191-8141(03)00043-9)
795

796 de Joussineau, G., Aydin, A., 2007. The evolution of the damage zone with fault growth in
797 sandstone and its multiscale characteristics. *J. Geophys. Res. Solid Earth* 112, 1–19.
798 <https://doi.org/10.1029/2006JB004711>
799

800 de Melo, M.S., Guimarães, G.B., Chinelatto, A.L., Giannini, P.C.F., Pontes, H.S., Chinelatto,
801 A.S.A., Atencio, D., 2015. Kaolinite, illite and quartz dissolution in the karstification of
802 Paleozoic sandstones of the Furnas Formation, Paraná Basin, Southern Brazil. *J. South Am.*
803 *Earth Sci.* 63, 20–35. <https://doi.org/10.1016/j.jsames.2015.06.011>
804
805 De Waele, J., Fabbri, S., Santagata, T., Chiarini, V., Columbu, A., Pisani, L., 2018.
806 Geomorphological and speleogenetical observations using terrestrial laser scanning and 3D
807 photogrammetry in a gypsum cave (Emilia Romagna, N. Italy). *Geomorphology* 319, 47–61.
808 <https://doi.org/10.1016/j.geomorph.2018.07.012>
809
810 De Waele, J., Plan, L., Audra, P., 2009. Recent developments in surface and subsurface karst
811 geomorphology: An introduction. *Geomorphology* 106, 1–8.
812 <https://doi.org/10.1016/j.geomorph.2008.09.023>
813
814 Dewever, B., Berwouts, I., Swennen, R., Breesch, L., Ellam, R.M., 2010. Fluid flow
815 reconstruction in karstified Panormide platform limestones (north-central Sicily): Implications
816 for hydrocarbon prospectivity in the Sicilian fold and thrust belt. *Mar. Pet. Geol.* 27, 939–958.
817 <https://doi.org/10.1016/j.marpetgeo.2009.10.018>
818
819 Dublyansky, Y., 2012. Hydrothermal caves, Second Edi. ed, *Encyclopedia of Caves*. Elsevier
820 Inc. <https://doi.org/10.1016/B978-0-12-383832-2.00055-4>
821
822 Dunham, R.J., 1962. Classification of Carbonate Rocks According to Depositional Textures.
823 *Classif. Carbonate Rocks--A Symp.*
824

825 Ennes-Silva, R.A., Bezerra, F.H.R., Nogueira, F.C.C., Balsamo, F., Klimchouk, A., Cazarin,
826 C.L., Auler, A.S., 2016. Superposed folding and associated fracturing influence hypogene
827 karst development in Neoproterozoic carbonates, São Francisco Craton, Brazil.
828 *Tectonophysics* 666, 244–259. <https://doi.org/10.1016/j.tecto.2015.11.006>
829

830 Evans, M.A., Fischer, M.P., 2012. On the distribution of fluids in folds: A review of
831 controlling factors and processes. *J. Struct. Geol.* 44, 2–24.
832 <https://doi.org/10.1016/j.jsg.2012.08.003>
833

834 Fabbri, S., Sauro, F., Santagata, T., Rossi, G., Waele, D., 2017. High-resolution 3-D mapping
835 using terrestrial laser scanning as a tool for geomorphological and speleogenetical studies in
836 caves: an example from the Lessini mountains (North Italy). *Geomorphology* 280, 16-29.
837 <https://doi.org/10.1016/j.geomorph.2016.12.001>
838

839 Fischer, M., Wilkerson, M.S., 2000. Predicting the orientation of joints from fold shape:
840 Results of pseudo – three-dimensional modeling and curvature analysis. *Geology* 28, 15-18.
841 [https://doi.org/10.1130/0091-7613\(2000\)28<15](https://doi.org/10.1130/0091-7613(2000)28<15)
842

843 Ford, D. C., and P. W. Williams (2007), *Karst Hydrogeology and Geomorphology*. John
844 Wiley & Sons Ltd, The Atrium, Southern Gate, Chichester. England.
845 <https://doi.org/10.1002/9781118684986>
846

847 Frumkin, A., 2013. New Developments of Karst Geomorphology Concepts. *Treatise*
848 *Geomorphol.* 6, 1–13. <https://doi.org/10.1016/B978-0-12-374739-6.00112-3>
849

850 Gholpoir, A.M., Cosgrove, J.W., Ala, M., 2016. New theoretical model for predicting and
851 modelling fractures in folded fractured reservoirs. *Pet. Geosci.* 22, 257–280.
852 <https://doi.org/10.1144/petgeo2013-055>
853

854 Gillespie, P.A., Howard, C.B., Walsh, J.J., Watterson, J., 1993. Measurement and
855 characterisation of spatial distributions of fractures. *Tectonophysics* 226, 113–141.
856 [https://doi.org/10.1016/0040-1951\(93\)90114-Y](https://doi.org/10.1016/0040-1951(93)90114-Y)
857

858 Giuffrida, A., La Bruna, V., Castelluccio, P., Panza, E., Rustichelli, A., Tondi, E., Giorgioni,
859 M., Agosta, F., 2019. Fracture simulation parameters of fractured reservoirs: Analogy with
860 outcropping carbonates of the Inner Apulian Platform, southern Italy. *J. Struct. Geol.* 123, 18–
861 41. <https://doi.org/10.1016/j.jsg.2019.02.007>
862

863 Goldscheider, N., 2005. Fold structure and underground drainage pattern in the alpine karst
864 system Hochifen-Gottesacker. *Eclogae Geol. Helv.* 98, 1–17. [https://doi.org/10.1007/s00015-](https://doi.org/10.1007/s00015-005-1143-z)
865 [005-1143-z](https://doi.org/10.1007/s00015-005-1143-z)
866

867 Guerriero, V., Iannace, A., Mazzoli, S., Parente, M., Vitale, S., Giorgioni, M., 2010.
868 Quantifying uncertainties in multi-scale studies of fractured reservoir analogues: Implemented
869 statistical analysis of scan line data from carbonate rocks. *J. Struct. Geol.* 32, 1271–1278.
870 <https://doi.org/10.1016/j.jsg.2009.04.016>
871

872 Guerriero, V., Vitale, S., Ciarcia, S., Mazzoli, S., 2011. Improved statistical multi-scale
873 analysis of fractured reservoir analogues. *Tectonophysics* 504, 14–24.
874 <https://doi.org/10.1016/j.tecto.2011.01.003>

875

876 Guimarães, J.T., Misi, A., Pedreira, A.J., Dominguez, J.M.L., 2011. The Bebedouro
877 Formation, Una Group, Bahia (Brazil). *Geol. Soc. Mem.* 36, 503–508.

878 <https://doi.org/10.1144/M36.47>

879

880 Jacquemyn, C., Swennen, R., Ronchi, P., 2012. Mechanical stratigraphy and (palaeo-)
881 karstification of the Murge area (Apulia, southern Italy). *Geol. Soc. London, Spec. Publ.* 370,
882 169–186. <https://doi.org/10.1144/SP370.4>

883

884 Kim, Y.S., Sanderson, D.J., 2010. Inferred fluid flow through fault damage zones based on
885 the observation of stalactites in carbonate caves. *J. Struct. Geol.* 32, 1305–1316.

886 <https://doi.org/10.1016/j.jsg.2009.04.017>

887

888 Klimchouk, A., 2009. Morphogenesis of hypogenic caves. *Geomorphology* 106, 100–117.

889 <https://doi.org/10.1016/j.geomorph.2008.09.013>

890

891 Klimchouk, A., Auler, A.S., Bezerra, F.H.R., Cazarin, C.L., Balsamo, F., Dublyansky, Y.,
892 2016. Hypogenic origin, geologic controls and functional organization of a giant cave system
893 in Precambrian carbonates, Brazil. *Geomorphology* 253, 385–405.

894 <https://doi.org/10.1016/j.geomorph.2015.11.002>

895

896 Klimchouk, A., Palmer, A.N., De Waele, J., Auler, A.S., Audra, P., 2017. Hypogene Karst
897 Regions and Caves of the World, *Cave and Karst Systems of the World*. Springer

898 International Publishing, Cham. <https://doi.org/10.1007/978-3-319-53348-3>

899

900 La Bruna, V., Agosta, F., Prosser, G., 2017. New insights on the structural setting of the
901 Monte Alpi area, Basilicata, Italy. *Ital. J. Geosci.* 136, 220–237.
902 <https://doi.org/10.3301/IJG.2017.03>
903
904 La Bruna, V., Agosta, F., Lamarche, J., Viseur, S., Prosser, G., 2018. Fault growth
905 mechanisms and scaling properties in foreland basin system: The case study of Monte Alpi,
906 Southern Apennines, Italy. *J. Struct. Geol.* 116, 94–113.
907 <https://doi.org/10.1016/j.jsg.2018.08.009>
908
909 La Bruna, V., Lamarche, J., Agosta, F., Rustichelli, A., Giuffrida, A., Salardon, R., Marié, L.,
910 2020. Structural diagenesis of shallow platform carbonates: Role of early embrittlement on
911 fracture setting and distribution, case study of Monte Alpi (Southern Apennines, Italy). *J.*
912 *Struct. Geol.* 131. <https://doi.org/10.1016/j.jsg.2019.103940>
913
914 Lamarche, J., Gauthier, B.D.M., Ondicolberry, G., Fleury, J.T., 2018. Fracture Corridors in
915 Fold and Thrust Zone, Devonian Sandstones Icla Syncline (Bolivia). In *Third EAGE*
916 *Workshop on Naturally Fractured Reservoirs* (Vol. 2018, No. 1, pp. 1-5). European
917 Association of Geoscientists & Engineers. <https://doi.org/10.3997/2214-4609.201800022>
918
919 Li, Y., Hou, G., Hari, K.R., Neng, Y., Lei, G., Tang, Y., Zhou, L., Sun, S., Zheng, C., 2018.
920 The model of fracture development in the faulted folds: The role of folding and faulting. *Mar.*
921 *Pet. Geol.* 89, 243–251. <https://doi.org/10.1016/j.marpetgeo.2017.05.025>
922
923 Ligtenberg, H., 2004. Fault seal analysis by enhancing fluid flow paths and fault irregularities
924 in seismic data. AAPG Int. Conf., October 24-27, 2004, Cancun, Mexico.

925

926 Lyu, X., Zhu, G., Liu, Z., 2020. Well-controlled dynamic hydrocarbon reserves calculation of
927 fracture–cavity karst carbonate reservoirs based on production data analysis. *J. Pet. Explor.*
928 *Prod. Technol.* 10, 2401–2410. <https://doi.org/10.1007/s13202-020-00881-w>

929

930 Marrett, R., Ortega, O.J., Kelsey, C.M., 1999. Extent of power-law scaling for natural
931 fractures in rock. *Geology* 27, 799–802. [https://doi.org/10.1130/0091-
932 7613\(1999\)027<0799:EOPLSF>2.3.CO](https://doi.org/10.1130/0091-7613(1999)027<0799:EOPLSF>2.3.CO)

933

934 Matthäi, S.K., Belayneh, M., 2004. Fluid flow partitioning between fractures and a permeable
935 rock matrix. *Geophys. Res. Lett.* 31, L07602 <https://doi.org/10.1029/2003GL019027>

936

937 Mazzoli, S., Ascione, A., Buscher, J.T., Pignalosa, A., Valente, E., Zattin, M., 2014. Low-
938 angle normal faulting and focused exhumation associated with late Pliocene change in
939 tectonic style in the southern Apennines (Italy). *Tectonics* 33, 1802–1818.

940 <https://doi.org/10.1002/2014TC003608>

941

942 Menezes, C., Martins Compan, A.L., Surmas, R., 2016. Permeability estimation using
943 ultrasonic borehole image logs in dual-porosity carbonate reservoirs. *Petrophysics* 57, 620–
944 637.

945

946 Miranda, T.S., Barbosa, J.A., Gale, J.F.W., Marrett, R., Gomes, I., Neumann, V.H.L.M.,
947 Matos, G.C., Correia, O.J., Alencar, M.L., 2014. Natural Fracture Characterization in Aptian
948 Carbonates, Araripe Basin, NE Brazil, in: 76th EAGE Conference & Exhibition. Amsterdam,
949 The Netherlands.

950

951 Misi, A., Veizer, J., 1998. Neoproterozoic carbonate sequences of the Una Group, Irecê

952 Basin, Brazil: chemostratigraphy, age and correlations. *Precambrian Res.* 89, 87–100.

953 [https://doi.org/10.1016/S0301-9268\(97\)00073-9](https://doi.org/10.1016/S0301-9268(97)00073-9)

954

955 Montaron, B., 2008. Confronting Carbonates, in: *Oil Review Middle East*. Abu Dhabi.

956

957 Morley, C.K., Warren, J., Tingay, M., Boonyasaknanon, P., Julapour, A., 2014. Comparison

958 of modern fluid distribution, pressure and flow in sediments associated with anticlines

959 growing in deepwater (Brunei) and continental environments (Iran). *Mar. Pet. Geol.* 55, 230–

960 249. <https://doi.org/10.1016/j.marpetgeo.2014.01.013>

961

962 Myers, R., Aydin, A., 2004. The evolution of faults formed by shearing across joint zones in

963 sandstone. *J. Struct. Geol.* 26, 947–966. <https://doi.org/10.1016/j.jsg.2003.07.008>

964

965 Mylroie, J.E., 2012. Coastal caves, Second Edi. ed, *Encyclopedia of Caves*. Elsevier Inc.

966 <https://doi.org/10.1016/B978-0-12-383832-2.00022-0>

967

968 Narasimhan, T.N., 2005. Hydrogeology in North America: Past and future. *Hydrogeol. J.* 13,

969 7–24. <https://doi.org/10.1007/s10040-004-0422-5>

970

971 Odling, N.E., Gillespie, P., Bourguine, B., Castaing, C., Chilés, J.P., Christensen, N.P., Fillion,

972 E., Genter, A., Olsen, C., Thrane, L., Trice, R., Aarseth, E., Walsh, J.J., Watterson, J., 1999.

973 Variations in fracture system geometry and their implications for fluid flow in fractured

974 hydrocarbon reservoirs. *Pet. Geosci.* 5, 373–384. <https://doi.org/10.1144/petgeo.5.4.373>

975

976 Odonne, F., Lézin, C., Massonnat, G., Escadeillas, G., 2007. The relationship between joint
977 aperture, spacing distribution, vertical dimension and carbonate stratification: An example
978 from the Kimmeridgian limestones of Pointe-du-Chay (France). *J. Struct. Geol.* 29, 746–758.
979 <https://doi.org/10.1016/j.jsg.2006.12.005>
980

981 Ogata, K., Senger, K., Braathen, A., Tveranger, J., Olausen, S., 2012. The importance of
982 natural fractures in a tight reservoir for potential CO₂ storage: a case study of the upper
983 Triassic–middle Jurassic Kapp Toscana Group (Spitsbergen, Arctic Norway). *Geol. Soc.*
984 *London, Spec. Publ.* 374, 395–415. <https://doi.org/10.1144/sp374.9>
985

986 Ogata, K., Senger, K., Braathen, A., Tveranger, J., 2014. Fracture corridors as seal-bypass
987 systems in siliciclastic reservoir-cap rock successions: Field-based insights from the Jurassic
988 Entrada Formation (SE Utah, USA). *J. Struct. Geol.* 66, 162–187.
989 <https://doi.org/10.1016/j.jsg.2014.05.005>
990

991 Ortega, O.J., Marrett, R.A., Laubach, S.E., 2006. A scale-independent approach to fracture
992 intensity and average spacing measurement. *Am. Assoc. Pet. Geol. Bull.* 90, 193–208.
993 <https://doi.org/10.1306/08250505059>
994

995 Palmer, A., 1990. Groundwater processes in karst terrains. In: Higgins C.G. & Coates D.R.
996 (Eds.), *Groundwater geomorphology; the role of subsurface water in Earth-Surface processes*
997 *and landforms. GSA Special Papers 252, 177-209.* <https://doi.org/10.1130/SPE252-p177>
998

999 Pantou, I., 2014. Impact of stratigraphic heterogeneity on hydrocarbon recovery in carbonate
1000 reservoirs: Effect of karst. Imperial College London.

1001

1002 Panza, E., Agosta, F., Zambrano, M., Tondi, E., Prosser, G., Giorgioni, M., Janiseck, J.M.,
1003 2015. Structural architecture and discrete fracture network modelling of layered fractured
1004 carbonates (Altamura Fm., Italy). *Ital. J. Geosci.* 134, 409–422.

1005 <https://doi.org/10.3301/IJG.2014.28>

1006

1007 Peacock, D.C.P., Shepherd, J., Peacock, D.C.P., 1997. Reactivated faults and transfer zones in
1008 the Southern Coalfield, Sydney Basin, Australia. *Aust. J. Earth Sci.* 44, 265–273.

1009 <https://doi.org/10.1080/08120099708728309>

1010

1011 Pollard, D.D., Aydin, A., 1988. Progress in understanding jointing over the past century.

1012 *Spec. Pap. Geol. Soc. Am.* 253, 313–336. <https://doi.org/10.1130/SPE253-p313>

1013

1014 Pollastro, R.M., 2003. Total Petroleum Systems of the Paleozoic and Jurassic, Greater
1015 Ghawar Uplift and Adjoining Provinces of Central Saudi Arabia and Northern Arabian-
1016 Persian Gulf U.S. Geological Survey Bulletin 2202-H Total Petroleum Systems of the
1017 Paleozoic and Jurassic, US Geological Survey 2202-H.

1018

1019 Pontes, C.C.C., Nogueira, F.C.C., Bezerra, F.H.R., Balsamo, F., Miranda, T.S., Nicchio,
1020 M.A., Souza, J.A.B., Carvalho, B.R.B.M., 2019. Petrophysical properties of deformation
1021 bands in high porous sandstones across fault zones in the Rio do Peixe Basin, Brazil. *Int. J.*

1022 *Rock Mech. Min. Sci.* 114, 153–163. <https://doi.org/10.1016/j.ijrmms.2018.12.009>

1023

1024 Popov, P., Qin, G., Bi, L., Efendiev, Y., Ewing, R., Kang, Z., Li, J., 2007. Multiscale methods
1025 for modeling fluid flow through naturally fractured carbonate karst reservoirs. Proc. - SPE
1026 Annu. Tech. Conf. Exhib. 6, 3714–3722. <https://doi.org/10.2523/110778-ms>
1027

1028 Questiaux, J.-M., Couples, G., Ruby, N., 2010. Fractured reservoirs with fracture corridors.
1029 Geophys. Prospect. 58, 279–295. <https://doi.org/1365-2478.2009.008140.x>
1030

1031 Railsback, L.B., 1998. Evaluation of spacing of stylolites and its implications for self-
1032 organization of pressure dissolution. J. Sediment. Res. 68, 2–7.
1033 <https://doi.org/10.2110/jsr.68.2>
1034

1035 Ramsay, J.G., 1967. Folding and Fracturing of Rocks. McGraw-Hill, New York, pp. 568.
1036

1037 Santos, R.F.V.C., Miranda, T.S., Barbosa, J.A., Gomes, I.F., Matos, G.C., Gale, J.F.W.,
1038 Neumann, V.H.L.M., Guimarães, L.J.N., 2015. Characterization of natural fracture systems:
1039 Analysis of uncertainty effects in linear scanline results. Am. Assoc. Pet. Geol. Bull. 99,
1040 2203–2219. <https://doi.org/10.1306/05211514104>
1041

1042 Segall, P., Pollard, D.P., 1983. Nucleation and growth of strike slip faults in granite. J.
1043 Geophys. Res. 88, 555–568. <https://doi.org/10.1029/JB088iB01p00555>
1044

1045 Souque, C., Knipe, R.J., Davies, R.K., Jones, P., Welch, M.J., Lorenz, J., 2019. Fracture
1046 corridors and fault reactivation: Example from the Chalk, Isle of Thanet, Kent, England. J.
1047 Struct. Geol. 122, 11–26. <https://doi.org/10.1016/j.jsg.2018.12.004>
1048

1049 Terzaghi, R.D., 1965. Sources of Error in Joint Surveys. *Géotechnique* 15, 287–304.

1050 <https://doi.org/10.1680/geot.1965.15.3.287>

1051

1052 Tian, F., Lu, X., Zheng, S., Zhang, H., Rong, Y., Yang, D., Liu, N., 2017. Structure and

1053 Filling Characteristics of Paleokarst Reservoirs in the Northern Tarim Basin, Revealed by

1054 Outcrop, Core and Borehole Images. *Open Geosci.* 9, 266–280. <https://doi.org/10.1515/geo->

1055 [2017-0022](https://doi.org/10.1515/geo-2017-0022)

1056

1057 Tian, F., Zhang, H., Zheng, S., Lei, Y., Rong, Y., Lu, X., Jin, Q., Zhang, L., Liu, N., 2015.

1058 Multi-layered ordovician paleokarst reservoir detection and spatial delineation: A case study

1059 in the Tahe Oilfield, Tarim Basin, Western China. *Mar. Pet. Geol.* 69, 53–73.

1060 <https://doi.org/10.1016/j.marpetgeo.2015.10.015>

1061

1062 Tisato, N., Sauro, F., Bernasconi, S.M., Bruijn, R.H.C., De Waele, J., 2012. Geomorphology

1063 Hypogenic contribution to speleogenesis in a predominant epigenic karst system: A case

1064 study from the Venetian Alps, Italy. *Geomorphology* 151–152, 156–163.

1065 <https://doi.org/10.1016/j.geomorph.2012.01.025>

1066

1067 Wang, X., Lei, Q., Lonergan, L., Jourde, H., Gosselin, O., Cosgrove, J., 2017. Heterogeneous

1068 fluid flow in fractured layered carbonates and its implication for generation of incipient karst.

1069 *Adv. Water Resour.* 107, 502–516. <https://doi.org/10.1016/j.advwatres.2017.05.016>

1070

1071 Warren, J., Morley, C.K., Charoentitirat, T., Cartwright, I., Ampaiwan, P., Khositichaisri, P.,

1072 Mirzaloo, M., Yingyuen, J., 2014. Structural and fluid evolution of Saraburi Group

1073 sedimentary carbonates, central Thailand: A tectonically driven fluid system. *Mar. Pet. Geol.*
1074 55, 100–121. <https://doi.org/10.1016/j.marpetgeo.2013.12.019>
1075
1076 Wilson, C.E., Aydin, A., Durlofsky, L.J., Sagy, A., Emily, E., Kreylos, O., Kellogg, L.H.,
1077 2011. From outcrop to flow simulation: Constructing discrete fracture models from a LIDAR
1078 survey. *Am. Assoc. Pet. Geol. Bull.* 95, 1883–1905. <https://doi.org/10.1306/03241108148>
1079
1080 Worthington, S.R.H., Ford, D.C., 1995. High sulfate concentrations in limestone springs: An
1081 important factor in conduit initiation? *Environ. Geol.* 25, 9–15.
1082
1083 Xu, X., Chen, Q., Chu, C., Li, G., 2017. Tectonic evolution and paleokarstification of
1084 carbonate rocks in the Paleozoic Tarim Basin. *Carbonates and Evaporites* 32, 487–496.
1085 <https://doi.org/10.1007/s13146-016-0307-4>
1086
1087 Zambrano, M., Tondi, E., Korneva, I., Panza, E., Agosta, F., Janiseck, J.M., Giorgioni, M.,
1088 2016. Fracture properties analysis and discrete fracture network modelling of faulted tight
1089 limestones, Murge Plateau, Italy. *Ital. J. Geosci.* 135, 55-67.
1090 <https://doi.org/10.3301/IJG.2014.42>
1091
1092 Zhao, K., Zhang, L., Zheng, D., Sun, C., Dang, Q., 2015. A reserve calculation method for
1093 fracture-cavity carbonate reservoirs in Tarim Basin, NW China. *Pet. Explor. Dev.* 42, 277–
1094 282. [https://doi.org/10.1016/S1876-3804\(15\)30017-3](https://doi.org/10.1016/S1876-3804(15)30017-3)
1095

1096 **Figure caption**

1097 Figure 1. (a) Sketch map of the São Francisco Craton Salitre formation; (b) zoom and location
1098 of the studied sites.

1099

1100 Figure 2. (a) Schematic stratigraphic column of the study area from Ioiô, Lapinha, Torrinha,
1101 and Paixão caves. (b) close up view of a grainstone; (c) photomicrograph of a representative
1102 mudstone with the pervasive occurrence of pyrite. (d) hand sample of mudstone with siltstone
1103 levels; (e) photomicrograph of mudstone that shows siliciclastic grains; (e) close up view of
1104 mudstone with chert nodules; (g) photomicrograph of a representative grainstone; Key: Un:
1105 stratigraphic unit described in the text, M: Mudstone, W: Wackestone, P: Packstone, G:
1106 Grainstone, F: Floatstone, Py: pyrite, Si: Silica, dol: dolomite, S0: bedding.

1107

1108 Figure 3. 3D model slice orthogonal to the cave passage in Ioiô cave showing different levels
1109 of dissolution due to distinct carbonate rock textures. The location of the slice is shown in Fig.
1110 7b. Key: FCZ: fracture corridor zone; HDZ: high-dissolution zone; SdB: Sedimentary breccia;
1111 MdSL: Mudstone with Silstone level; Md: mudstone; St: stalactites.

1112

1113 Figure 4. (a) View of the Ioiô cave roof displaying speleothems aligned along the main N-S-
1114 and E-W-striking fracture zones; (b) Orthogonal system of fractures on the cave ceiling; (c)
1115 gentle fold highlighting the high dissolution zone along the fold hinge. Note opposite bedding
1116 dips. Key: HDZ: high-dissolution zone.

1117

1118 Figure 5. (a) outcrop view of an external wall near Lapinha cave entrance; (b) linedrawing of
1119 (a); (c) lower hemisphere equal-area projections of the poles related to the NSB and SB; (d)
1120 close up view of a karst dissolution zone parallel to a persistent non-stratabound fracture zone
1121 inside the cave. Key: NSB = Non-Stratabound fracture; S0 = bedding.

1122

1123 Figure 6. Close up view of fracture sets in the ceiling of caves: (a) E-W-striking fracture set
1124 abuts against N-S-striking fracture set in the Torrinha cave; (b) bed-parallel stylolite and
1125 bedperpendicular folded vein in the Ioiô cave; (c) normal fault with left-lateral strike-slip
1126 kinematics in the Lapinha cave; (d) line drawing of (c).

1127

1128 Figure 7. Structural and karst features of the Ioiô cave: (a) cave map with area surveyed with
1129 LiDAR; (b) 3D LiDAR model of the cave with the location of investigated sites; (c) main fold
1130 hinges of the cave; (d) lower hemisphere equal-area projection of the poles and relative density
1131 contour plots of bedding planes and fractures; (e) digital image of the slice on site B showing a
1132 high dissolution zone along a fracture corridor following the fold hinge in the central part of
1133 the cave passage; (f) detail of HDZ highlighted in (e) (yellow square). Key: FCZ: fracture
1134 corridor zone; HDZ: high-dissolution zone.

1135

1136 Figure 8. Structural and karst features of the Lapinha cave: (a) cave map with area surveyed
1137 with LiDAR; (b) 3D model of the cave with the location of investigated sites; (c) structural map
1138 of the central part of the cave showing two main directions of anticline folds (d) lower
1139 hemisphere equalarea projection of the poles of NSB and SB fractures, mean bedding planes,
1140 and mean fold hinge (black dot); (e) digital slice between the (C) and (I) sites highlighting the
1141 wavelength of N-S folds. Key: FCZ: fracture corridor zone.

1142

1143 Figure 9. Geometric features of the Torrinha (a-d) and Paixão (e) caves: (a) internal view of the
1144 cave geometry showing widening of the passage along the fold hinge; (b) 3D LiDAR model
1145 (a); (c) plan view of the site (e) (location in Fig. 9b) showing both major N-S- and subsidiary
1146 E-W-oriented cave passages; (d) transversal view of (d) showing the vertical elliptical shape of

1147 the cave passages; (e) 3D LiDAR model of Paixão cave ceiling with a close up view of two N-
1148 S- and E-W-string fracture sets.

1149

1150 Figure 10. Structural and dissolutional features of the Torrinha cave: (a) map highlighting the
1151 LiDAR surveyed area in the southern portion of the cave; (b) 3D model of the scanned areas
1152 with the location of investigated sites; (c) structural map of site B in the cave; (d) lower
1153 hemisphere equal-area projection of the poles of NSB and SB fractures, mean bedding planes,
1154 and mean fold hinge (black dot). (e) NW-SE strike-slip fault at site B of Torrinha cave.

1155

1156 Figure 11. Structural and dissolutional features of the Paixão cave: (a) map highlighting the
1157 area surveyed with LiDAR and location of the investigated sites; (b) 3D LiDAR model of the
1158 studied part of the cave; (c) structural map of the eastern part of the Paixão cave highlighting
1159 the en echelon pattern of fold hinges; (d) lower hemisphere equal-area projection of the poles
1160 of NSB and SB fractures, mean bedding planes, and mean fold hinge (black dot); (e) zoom on
1161 the central portion of the model highlighting the location of a fault zone (blue ellipsoid); (f)
1162 digital slice of the cave's central portion affected by a dip-slip fault zone; (g) orthogonal-to-dip
1163 view of a normal fault located in the central portion of the cave; (h) cave central portion
1164 highlighting the fault displayed in (e). Key: HD = High displacement; St = stalactite.

1165

1166 Figure 12. Quantitative data of the Ioiô site: (a) Outcrop oblique view of the site and the
1167 investigated beds; red lines used for the linedrawings are related to both SB and NSB fractures;
1168 (b) Lower hemisphere equal-area projection of the poles and relative density contour plots
1169 representing the fractures measured in the site; (c) Log-log diagrams of the cumulative
1170 frequency distribution for fracture spacing; blue lines correspond to exponential-law

1171 distribution, red lines correspond to power-law distribution calculated for the single fracture
1172 sets in the site.

1173

1174 Figure 13. Quantitative data in the Lapinha site: (a) Outcrop view of beds; red lines used for
1175 the linedrawing are related to both SB and NSB fracture sets; (b) Lower hemisphere equal-area
1176 projection of poles and relative density contour plots representing fractures; (c) Log-log
1177 diagram of the cumulative frequency distribution for fracture spacing; blue lines correspond to
1178 exponentiallaw distribution, red lines correspond to power-law distribution calculated for the
1179 single fracture sets.

1180

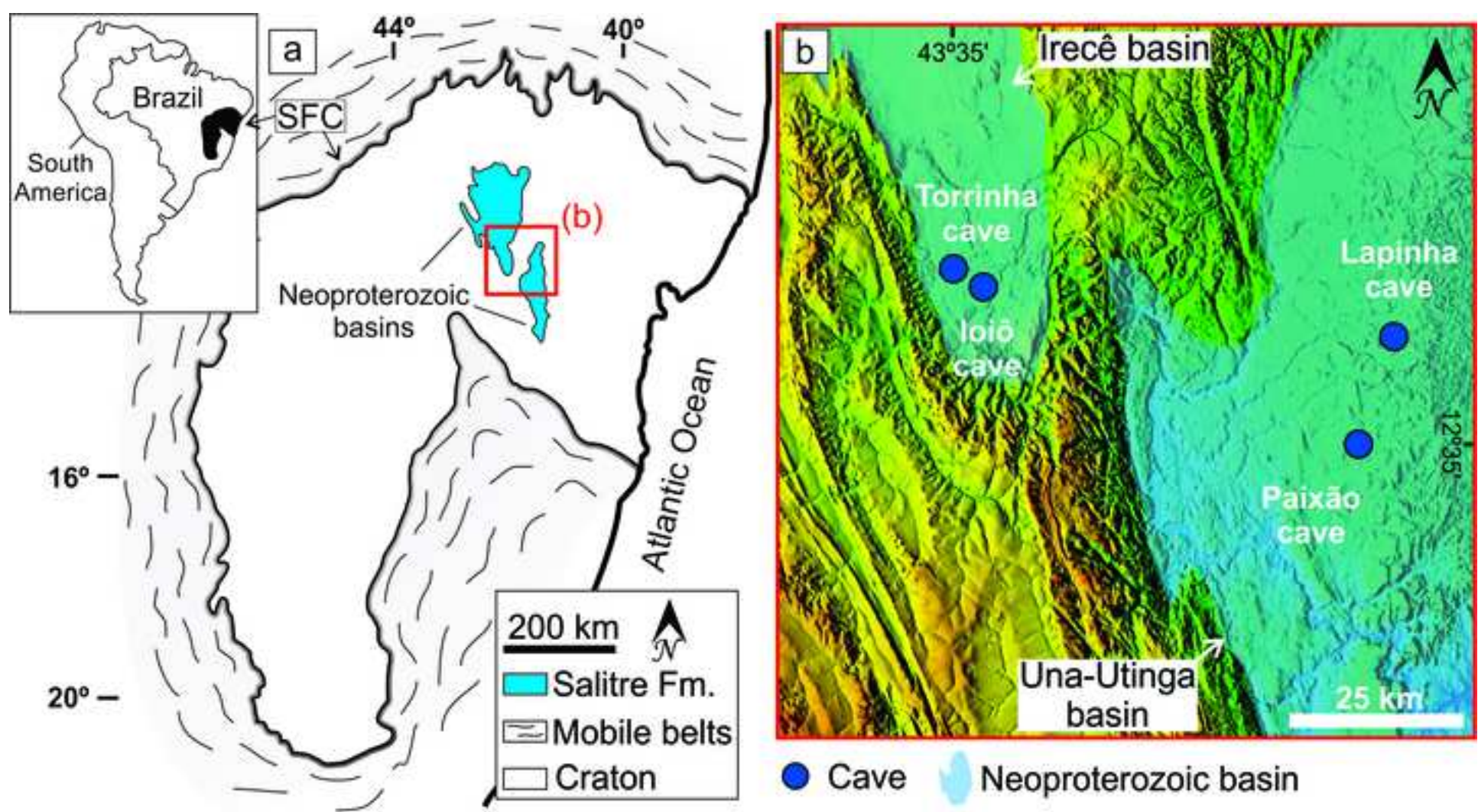
1181 Figure 14. Quantitative structural data of the Torrinha site: (a) Outcrop view of the investigated
1182 beds outside the cave; red lines used for the linedrawing are related to both SB and NSB
1183 fractures; (b) lower hemisphere equal-area projection of the poles and relative density contour
1184 plots representing the fractures; (c) log-log diagrams of the cumulative frequency distribution
1185 for fracture spacing; blue lines correspond to exponential law distribution and red lines
1186 correspond to power-law distribution calculated for the single fracture sets in the site.

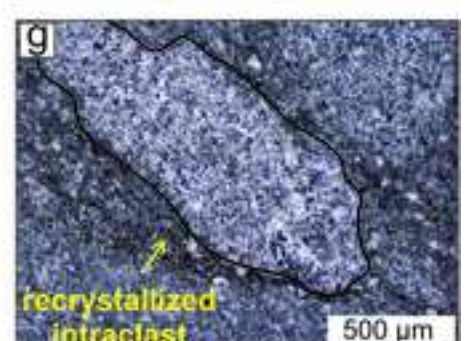
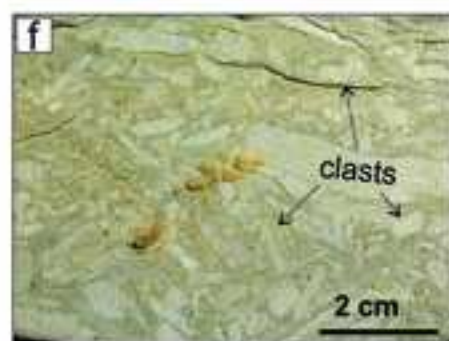
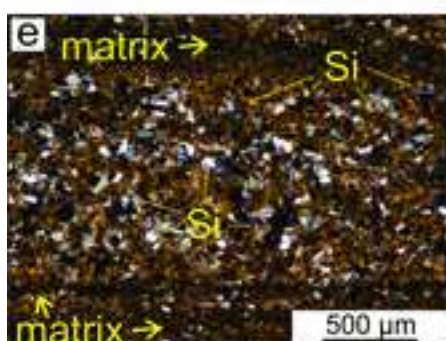
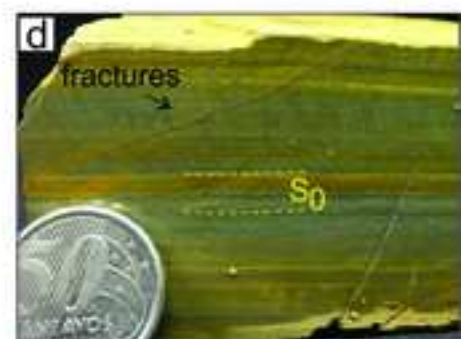
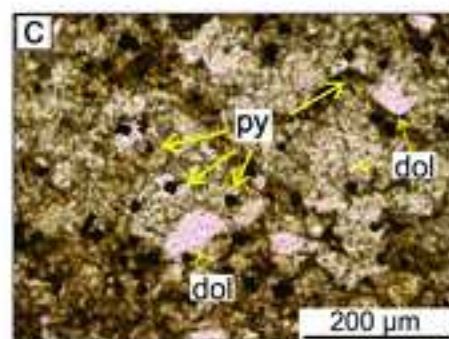
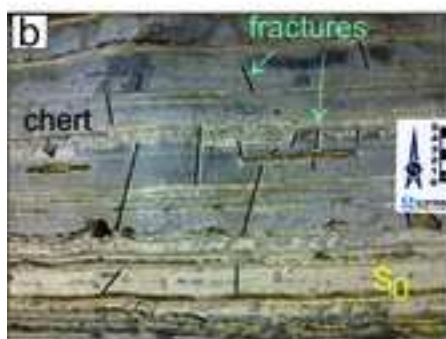
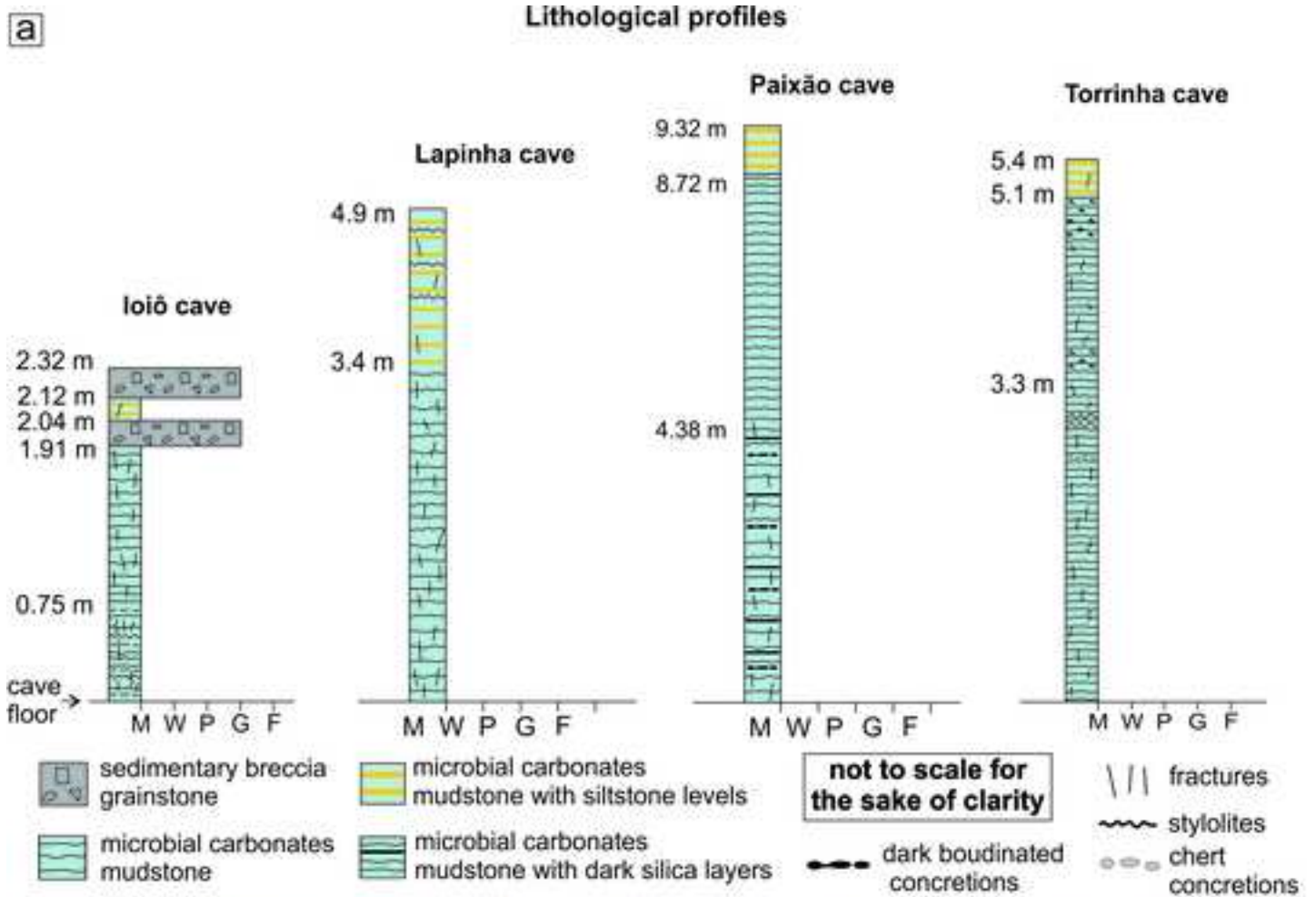
1187

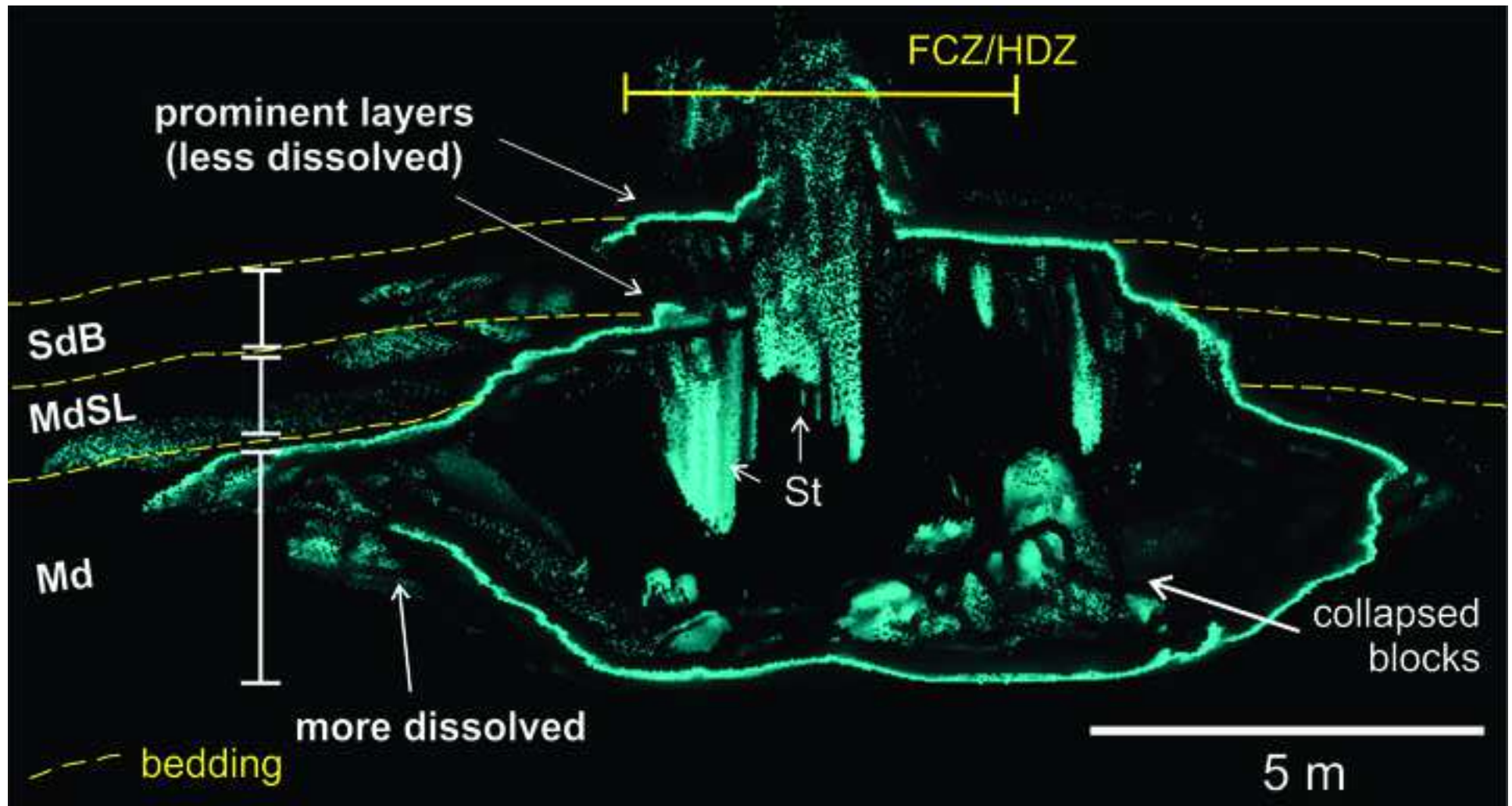
1188 Figure 15. Quantitative data for the Paixão site: (a) lower hemisphere equal-area projection of
1189 the poles and relative density contour plots representing the fractures; (b) log-log diagram of
1190 the cumulative frequency distribution for fracture spacing; blue lines correspond to exponential-
1191 law distribution; red lines correspond to power-law distribution calculated for the single fracture
1192 sets in the site.

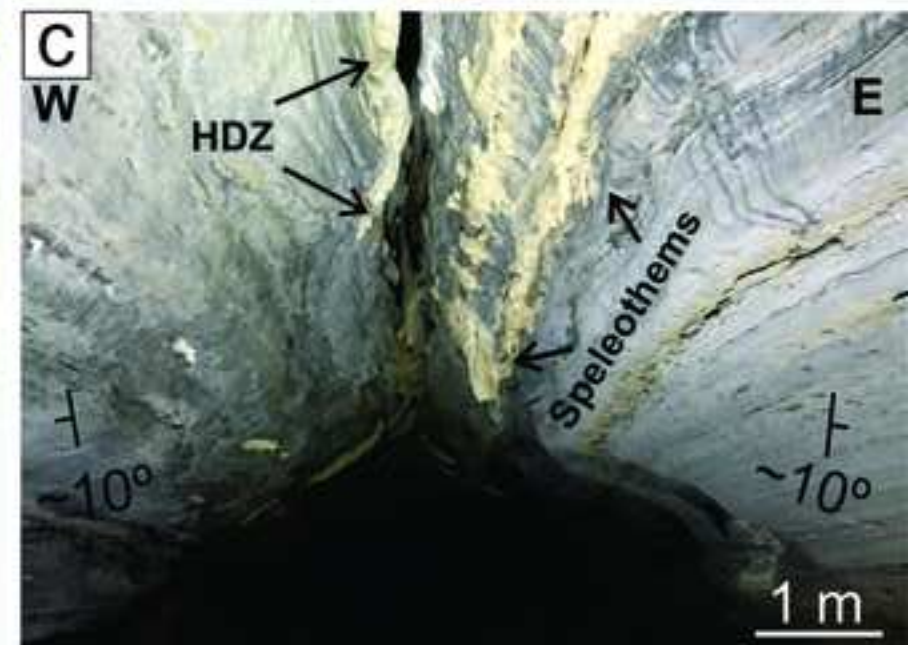
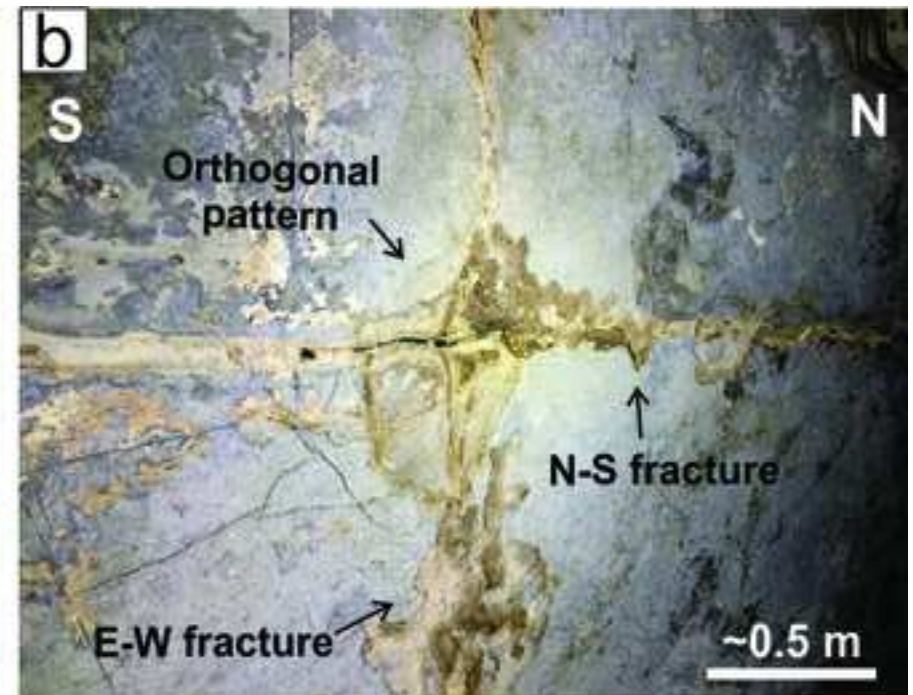
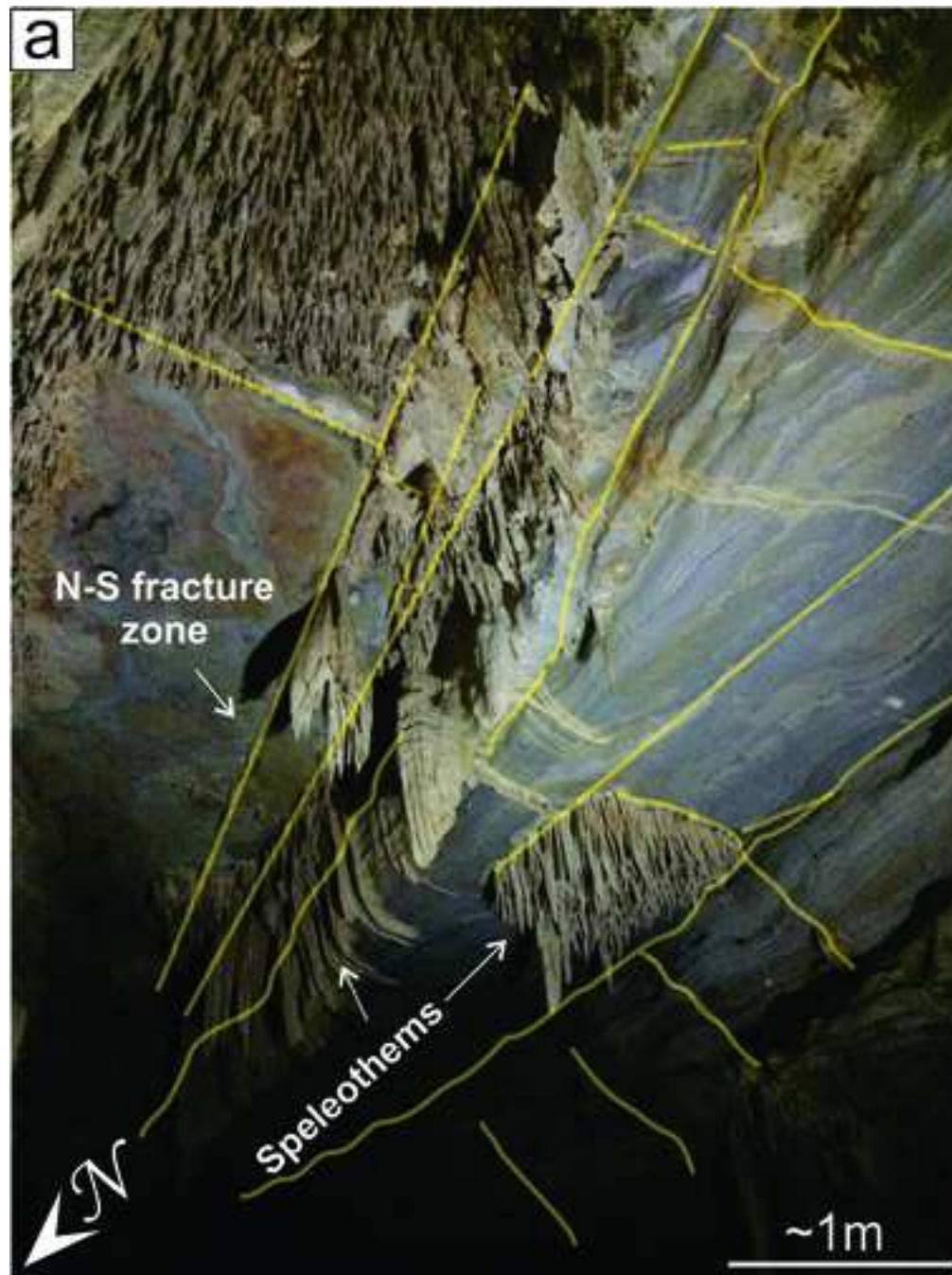
1193

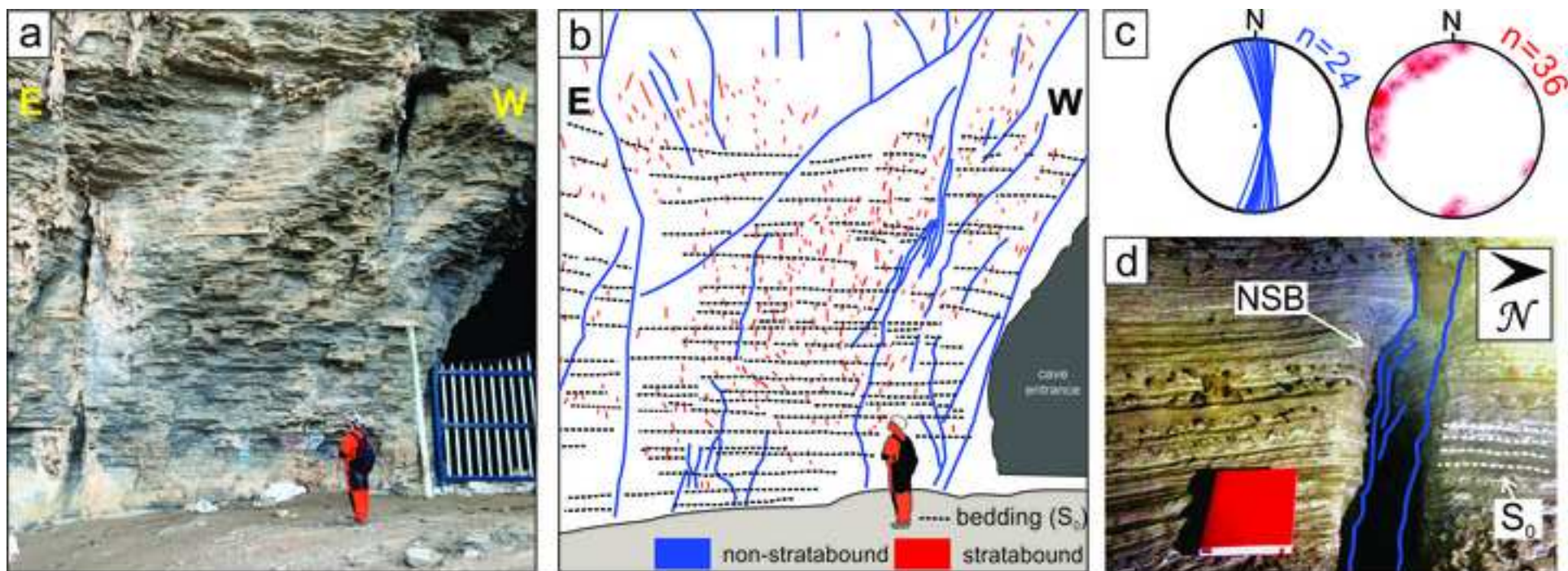
1194 Figure 16. Evolutionary conceptual model proposed for development of the hypogenic conduits
1195 in carbonate units of the Salitre Formation, Brazil. (a) background burial-related; (b) E-W
1196 compression; (c) N-S compression; (d) ascending fluids and karst development

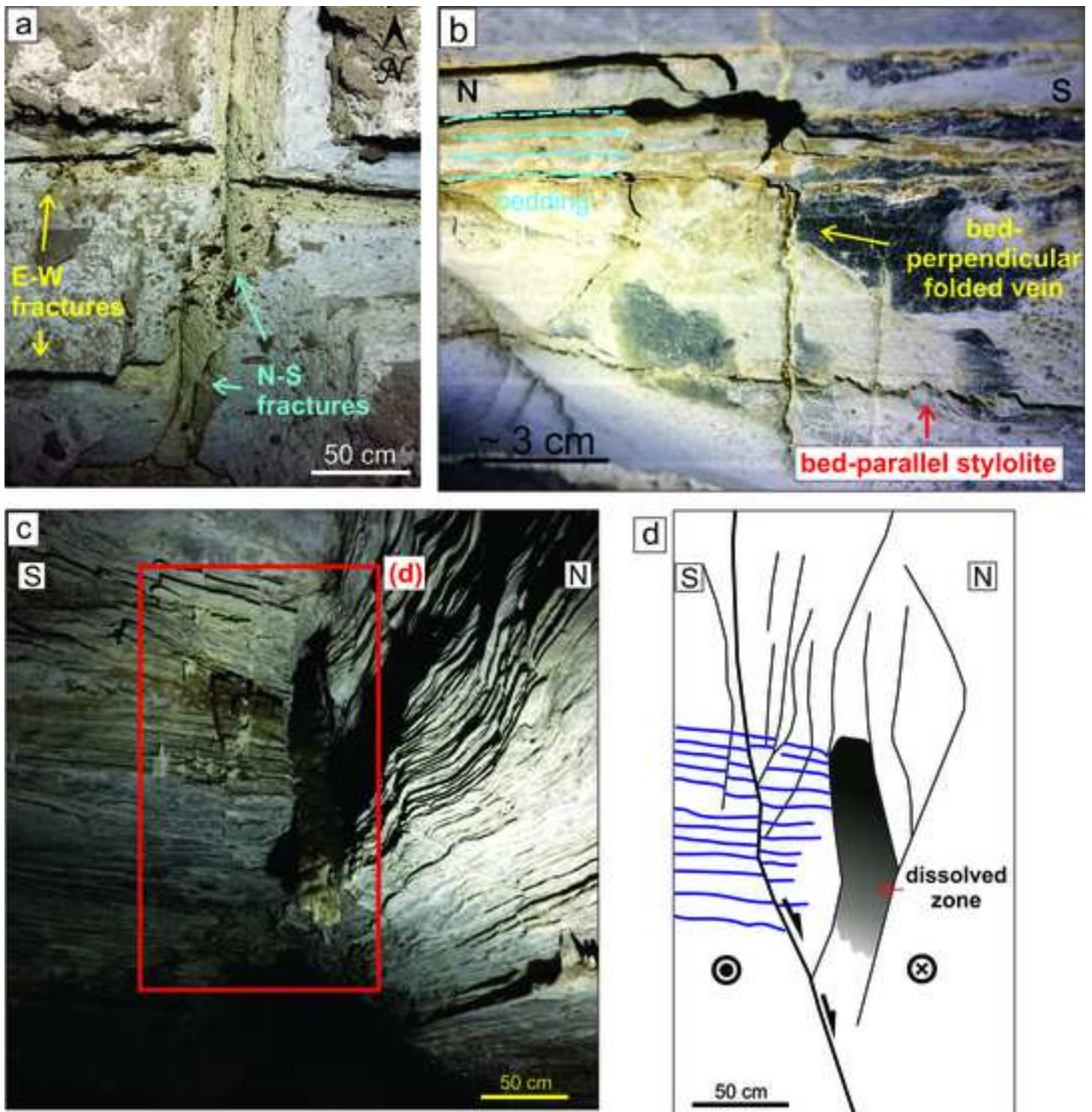


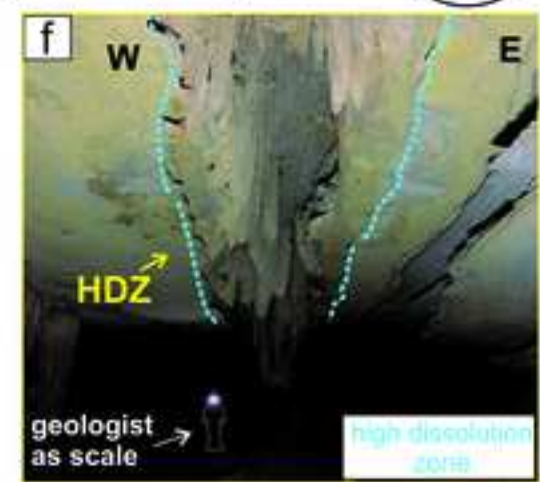
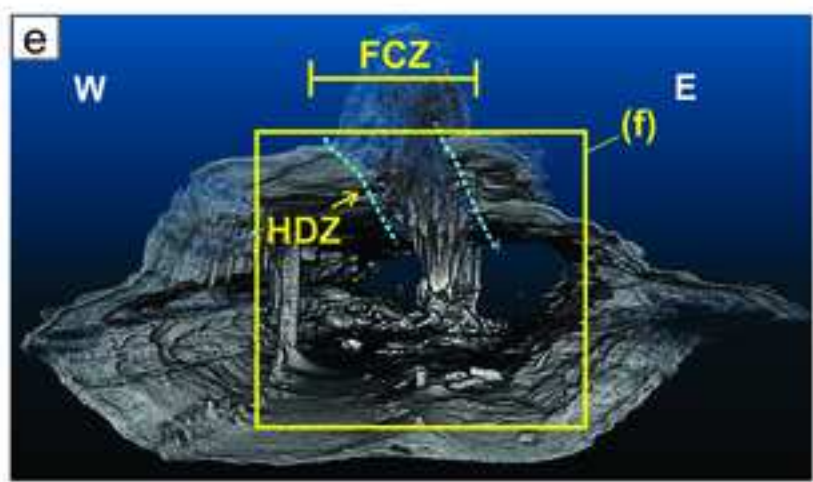
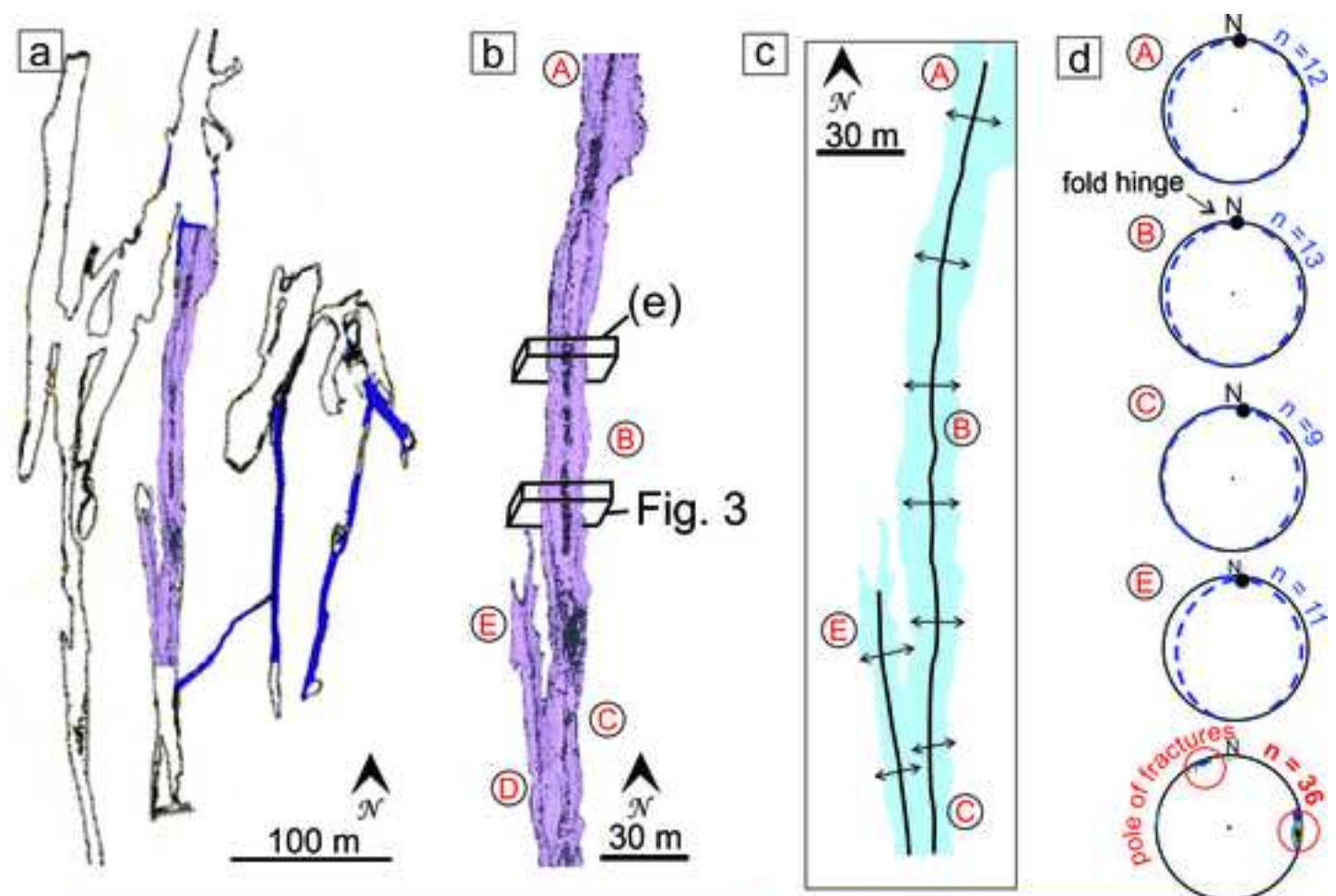


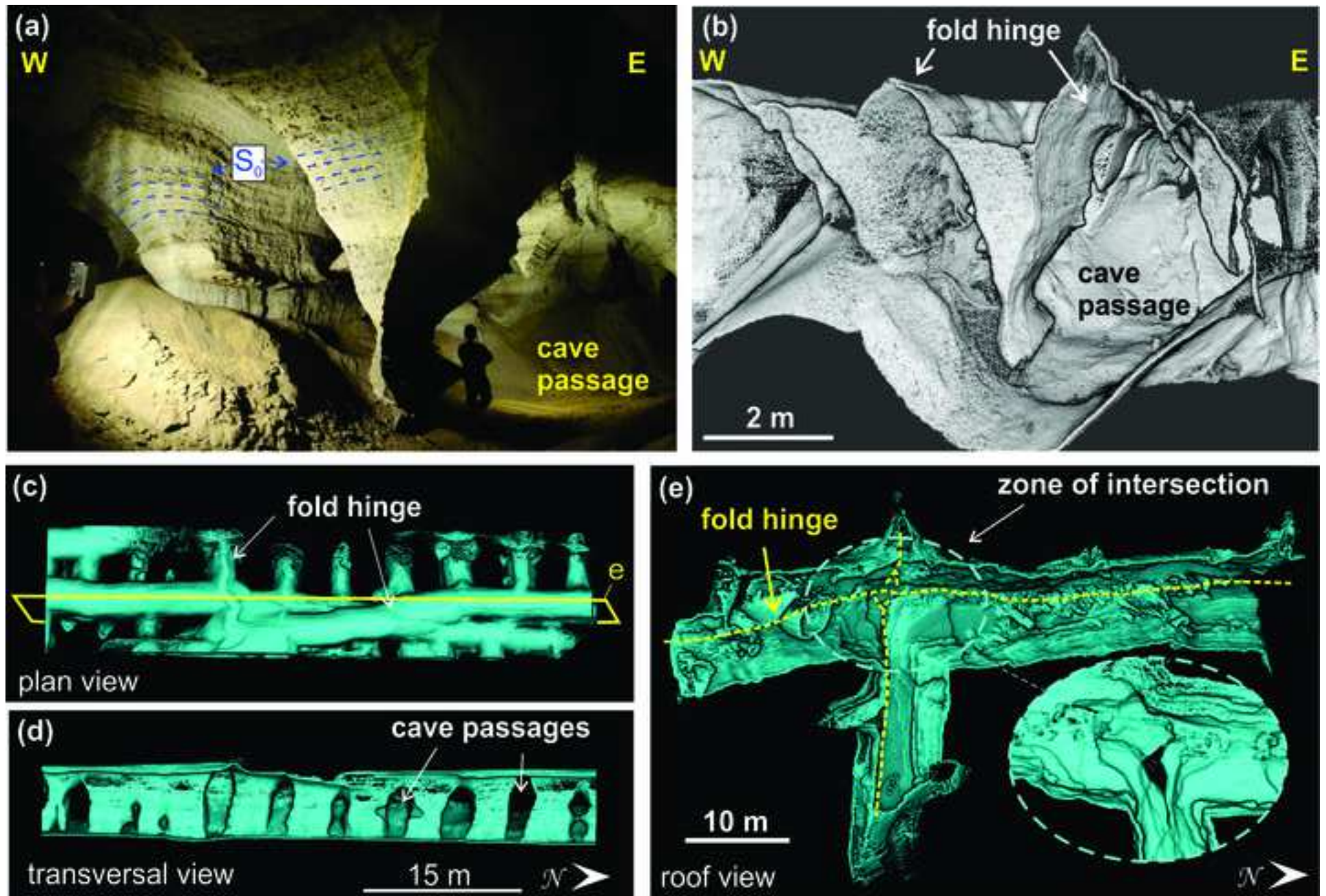


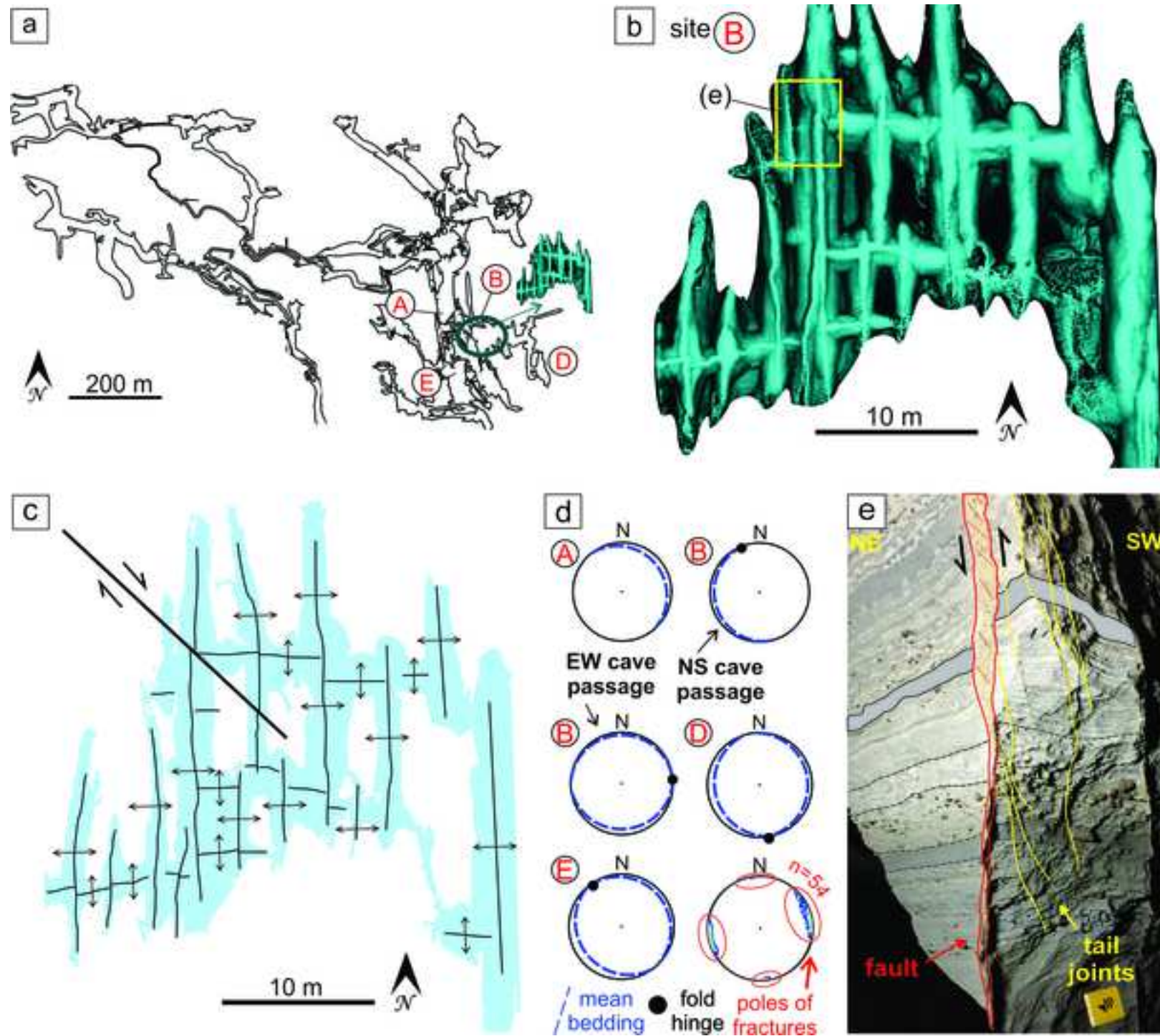


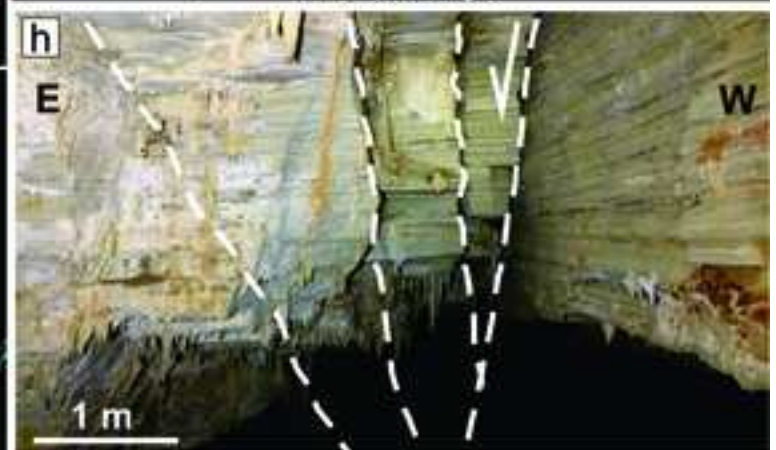
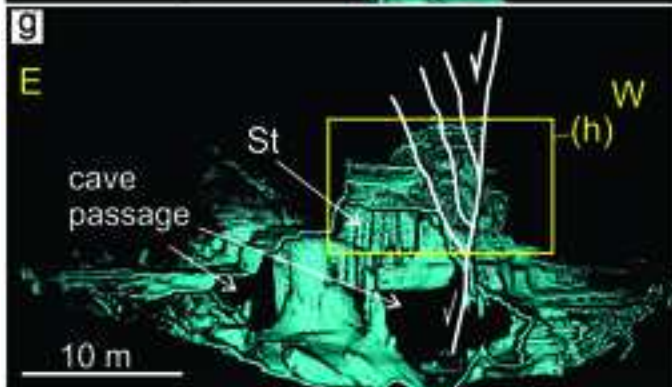
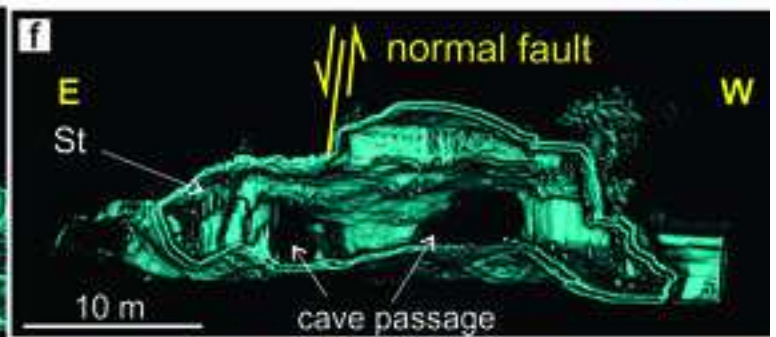
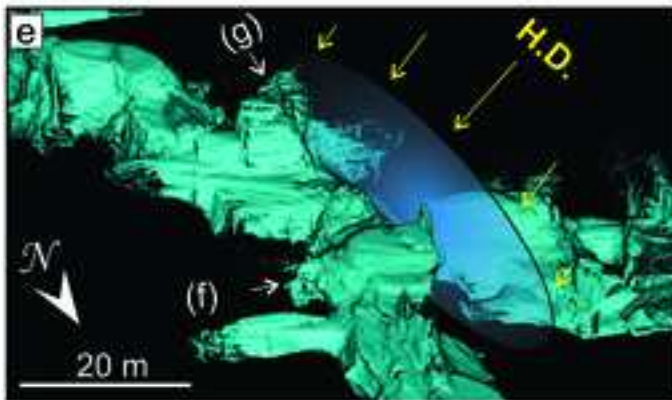
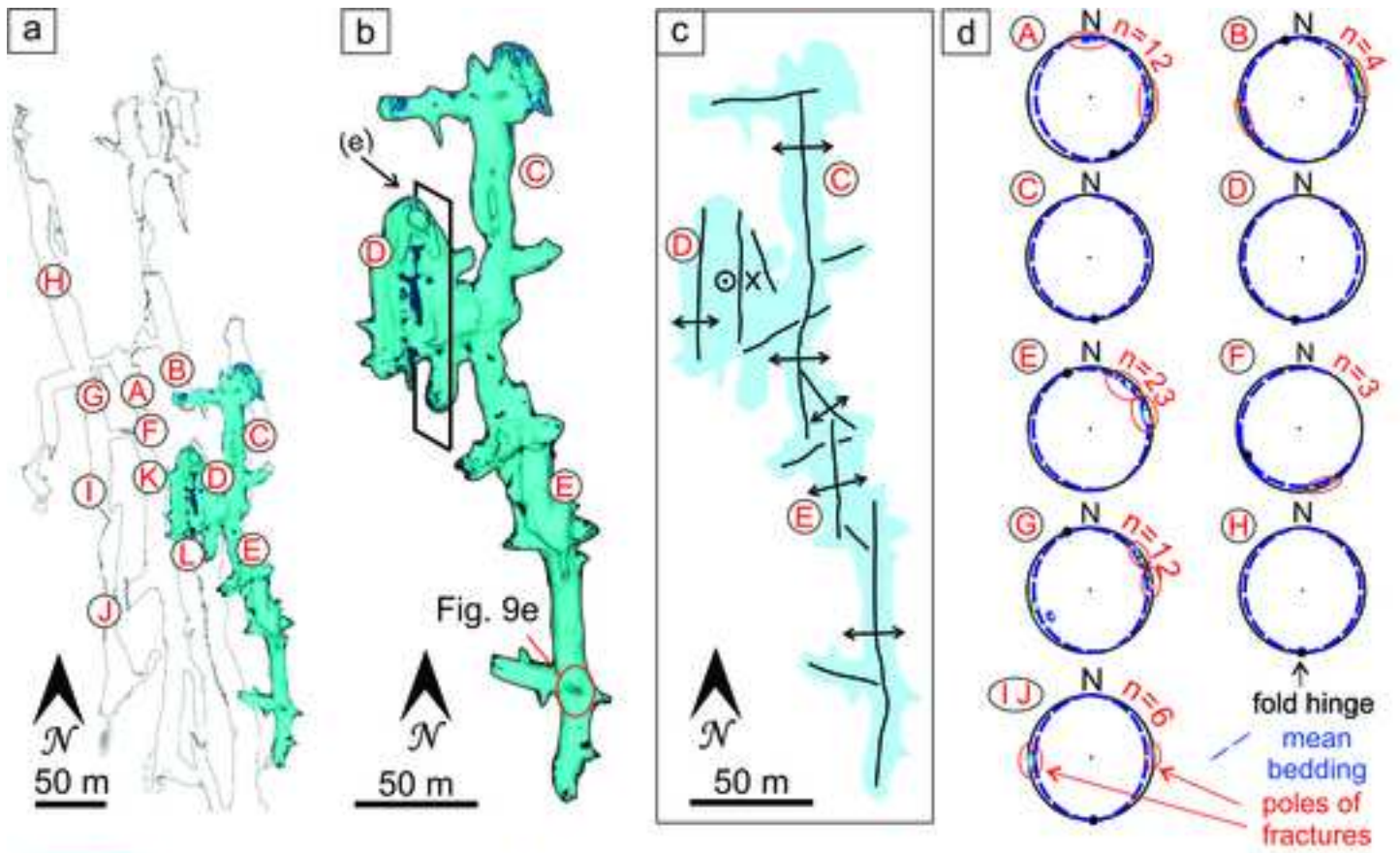


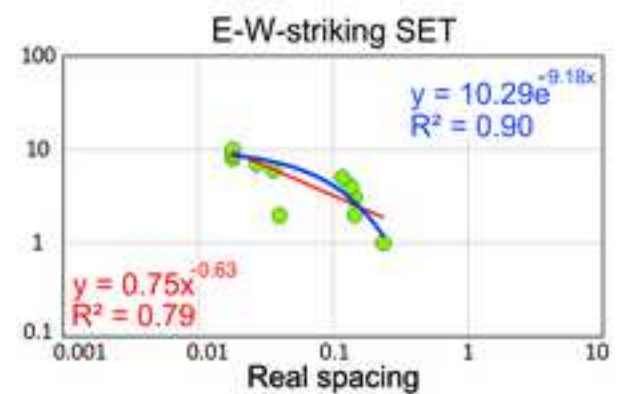
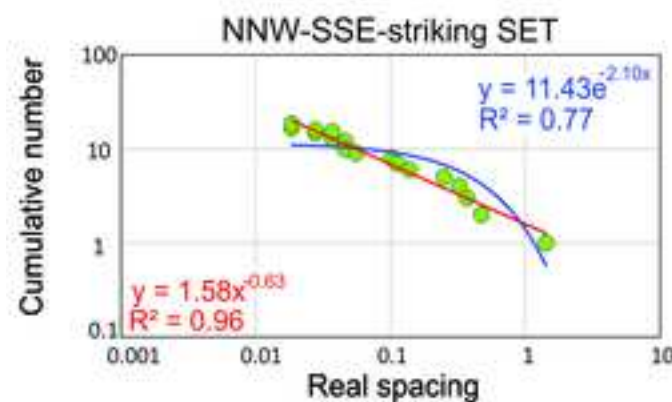
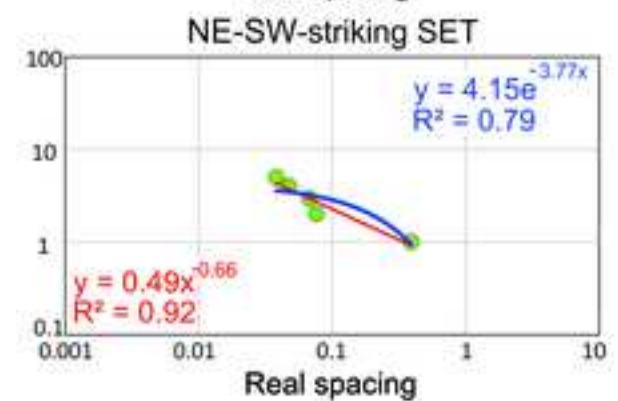
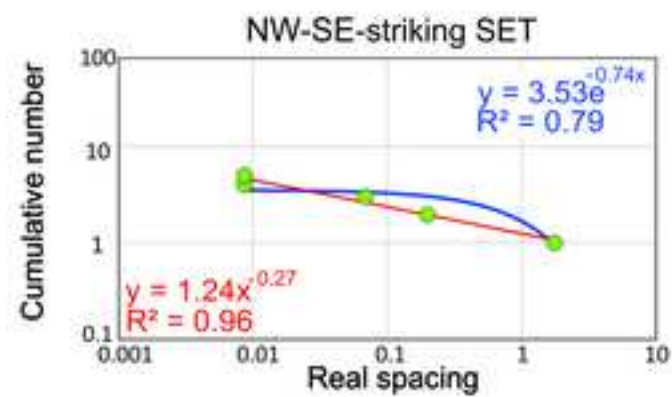
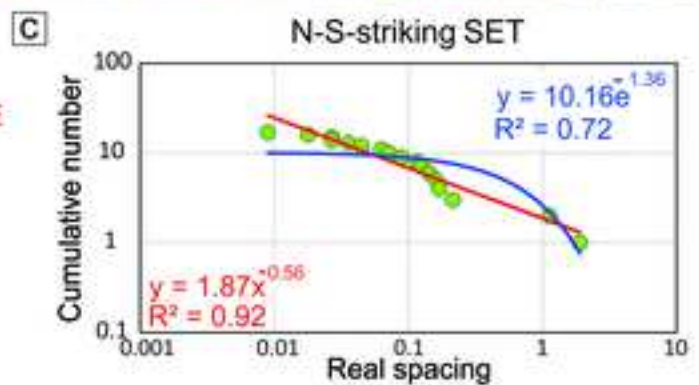
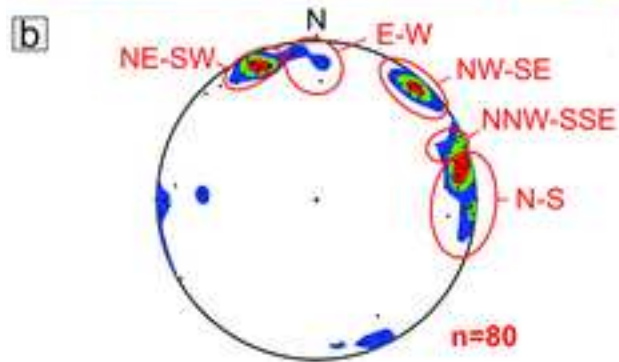
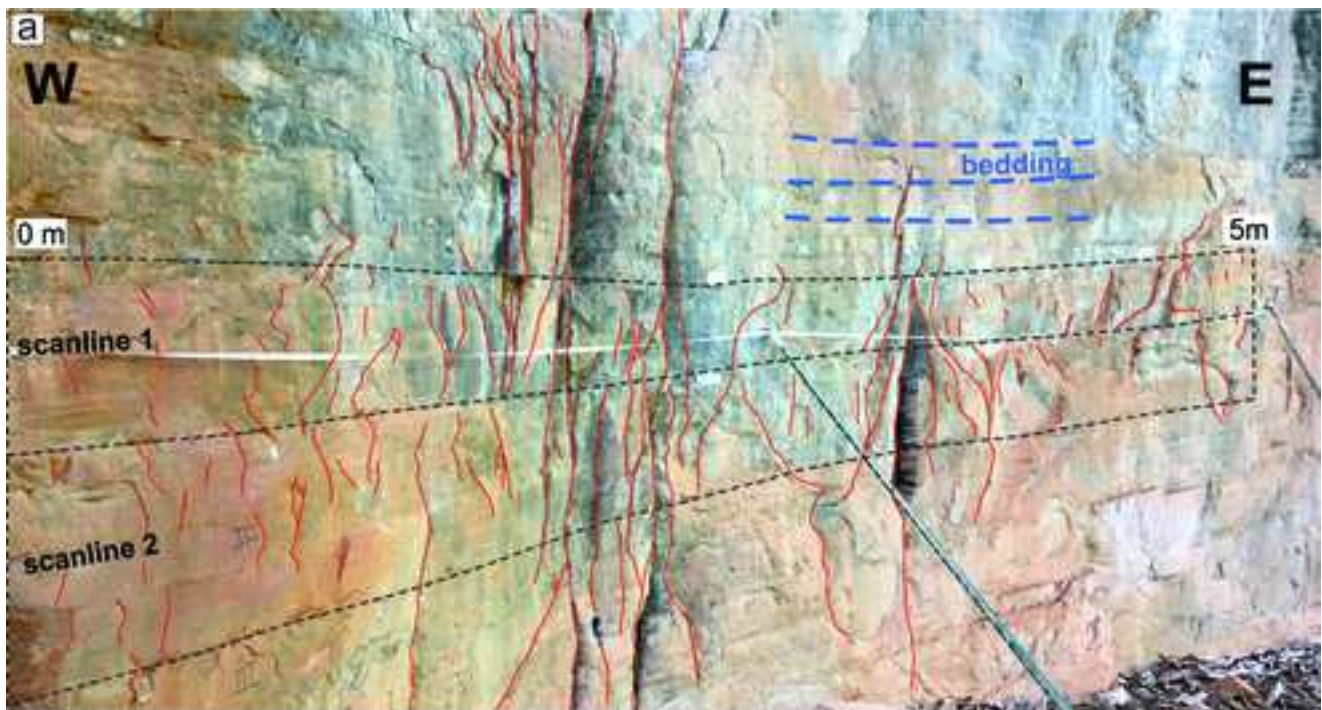


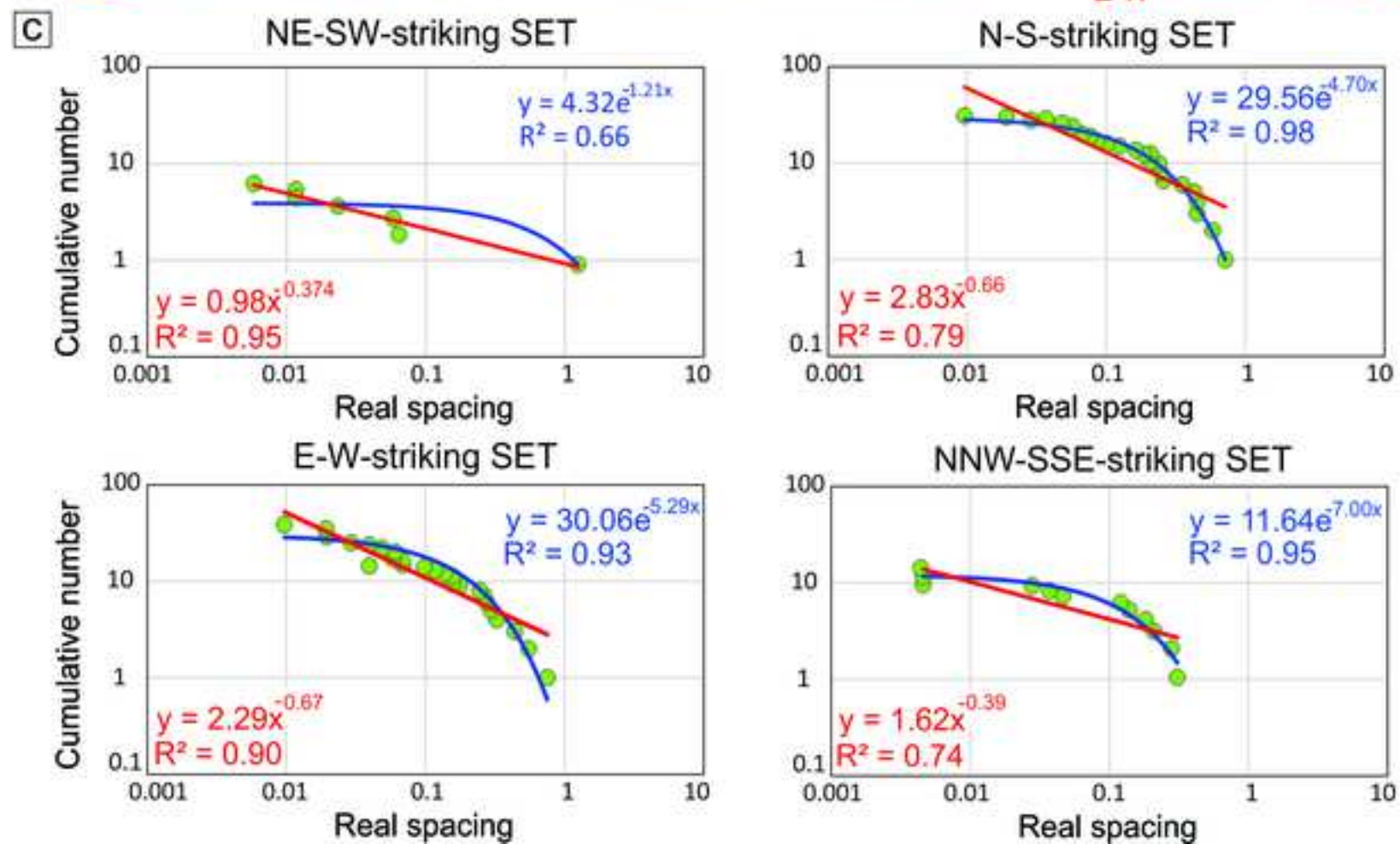


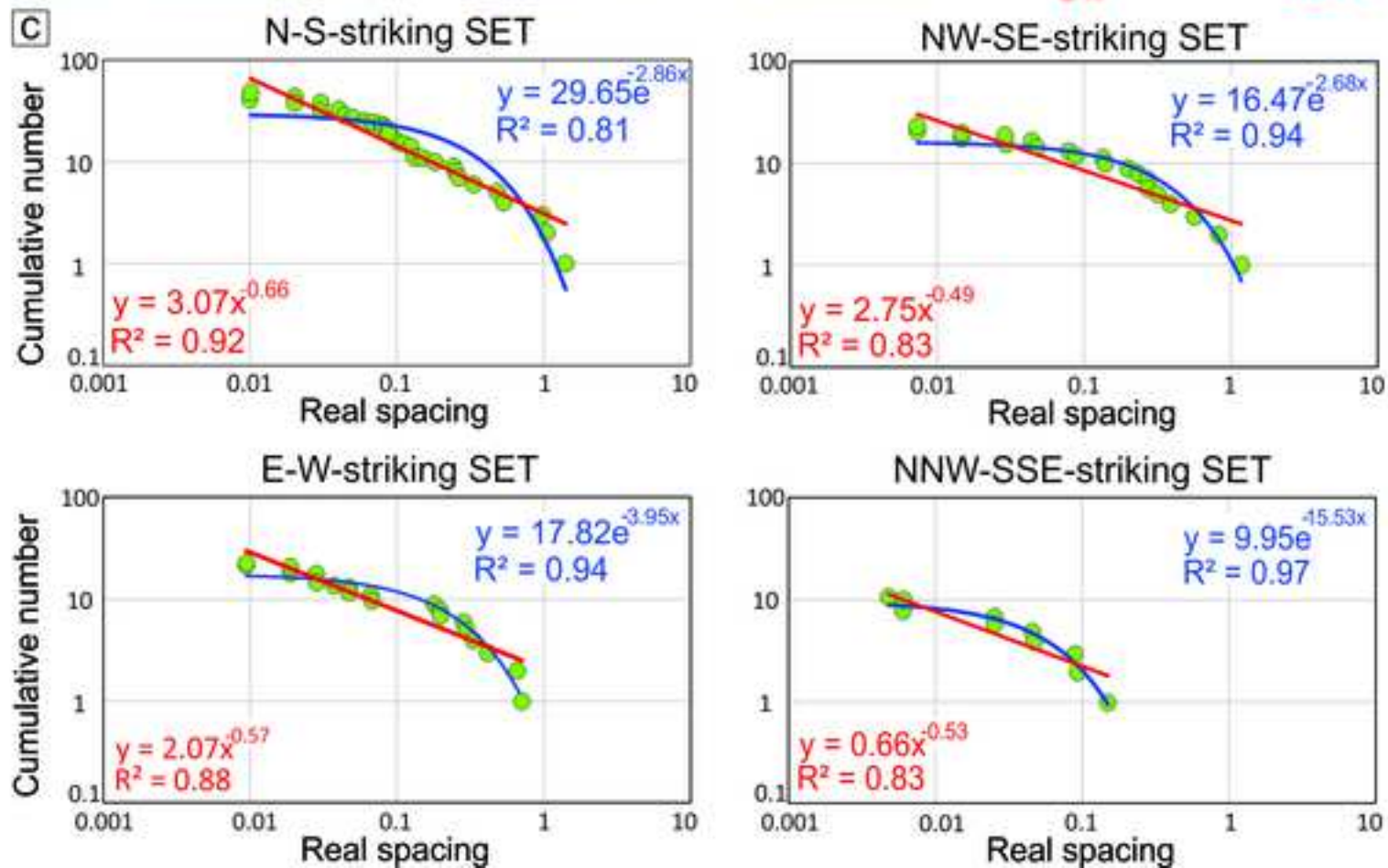


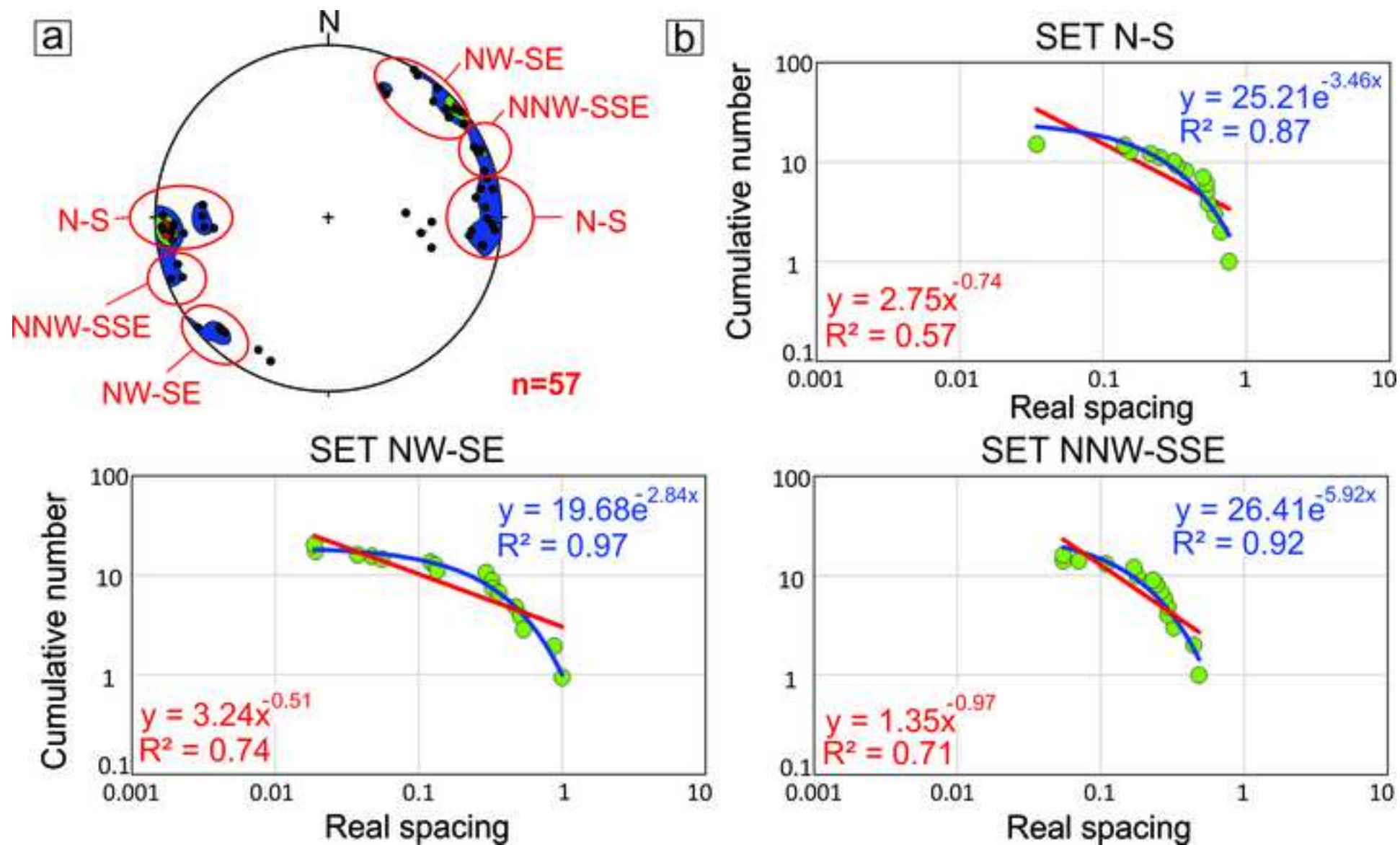


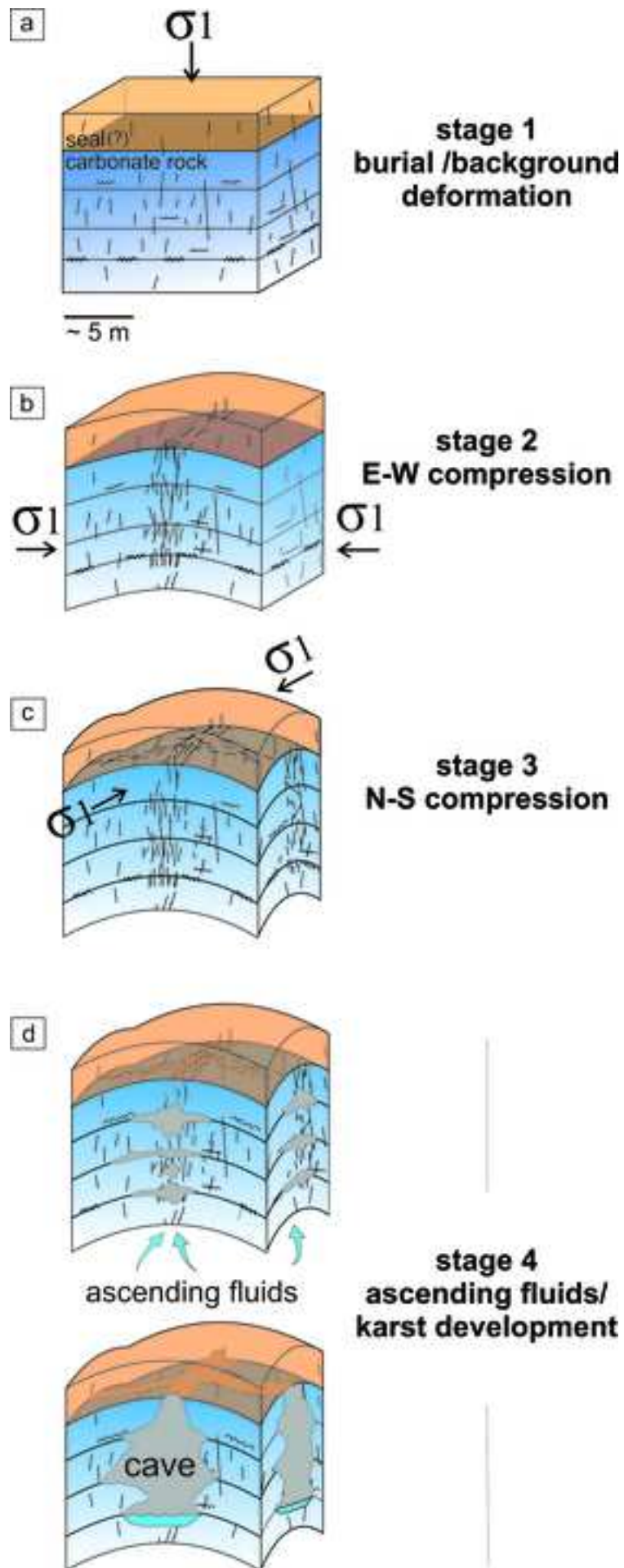














Click here to access/download

Table

Table 1.docx



Declaration of interests

The authors declare that they have no known competing financial interests or personal relationships that could have appeared to influence the work reported in this paper.

The authors declare the following financial interests/personal relationships which may be considered as potential competing interests: